

DOKUZ EYLÜL UNIVERSITY
GRADUATE SCHOOL OF NATURAL AND APPLIED SCIENCES

**DESIGN, IMPLEMENTATION AND
EVALUATION OF COMPUTER LABORATORY
EXPERIMENTS FOR MEDICAL IMAGING
SYSTEMS ON A SINGLE OBJECT**

by

Mazlum UNAY

December, 2021

İZMİR

**DESIGN, IMPLEMENTATION AND
EVALUATION OF COMPUTER LABORATORY
EXPERIMENTS FOR MEDICAL IMAGING
SYSTEMS ON A SINGLE OBJECT**

**A Thesis Submitted to the
Graduate School of Natural and Applied Sciences Dokuz Eylül University
In Partial Fulfilment of the Requirements for the Degree of Master of Science
in Biomedical Technologies**

**by
Mazlum UNAY**

**December, 2021
İZMİR**

M.Sc THESIS EXAMINATION RESULT FORM

We have read this thesis entitled “**DESIGN, IMPLEMENTATION AND EVALUATION OF COMPUTER LABORATORY EXPERIMENTS FOR MEDICAL IMAGING SYSTEMS ON A SINGLE OBJECT**” completed by **MAZLUM UNAY** under supervision of **ASSOC. PROF. DR. MUSTAFA ALPER SELVER** and we certify that in our opinion it is fully adequate, in scope and in quality, as a thesis for the degree of Master of Science.

.....
Assoc. Prof. Dr. Mustafa Alper SELVER

Supervisor

.....
Prof. Dr. Oğuz Dicle

.....
Assist. Prof. Dr. M. Zübeyir Ünlü

.....
(Jury Member)

.....
(Jury Member)

.....
Prof. Dr. Okan FISTIKOĞLU

Director

Graduate School of Natural and Applied Sciences

ACKNOWLEDGEMENTS

My sincere thanks,

To my academic advisor M.Alper SELVER for his guidance,

To my family for their confidence in me and their unconditional support all time,

To my fellows for their great friendship.

Mazlum UNAY



**DESIGN, IMPLEMENTATION AND EVALUATION OF COMPUTER
LABORATORY EXPERIMENTS FOR MEDICAL IMAGING SYSTEMS ON
A SINGLE OBJECT**

ABSTRACT

Medical imaging systems (MIS), a crucial aspect of the electrical and electronics engineering (EEE) curriculum, encompasses a wide range of approaches, including physics, instrumentation, data gathering, image production, modeling, and quality evaluation. Although many EEE curricula include a well-structured MIS course that introduces students to all contemporary diagnostic imaging systems, MIS laboratory work is confined to image processing.

In this thesis, a set of laboratory experiments has been designed in order to increase the applicability and understanding of studies related to MIS. The functioning of conventional X-ray, Computed Tomography (CT), and Magnetic Resonance Imaging (MRI) modalities are simulated by utilizing the Shepp-Logan phantom. Traditional biomedical image acquisition techniques have been analyzed using the same phantom to facilitate an understanding of their differences and similarities. Through simulations for each modality, a hands-on learning strategy for imaging systems is developed.

In the developed experimental procedures, multiple states can be displayed for each imaging system by using adjustable parameters during the simulation of each modality through algorithms created for each specific case. All conceivable scenarios are aimed to be simulated. The acquired outcomes offer the possibility of comparing the different modalities as well as various conditions of the imaging systems. The content consists of projection and back-projection for X-ray radiography and CT, while k-space is described processed and several reconstruction methods are analyzed for MRI.

Keywords: Computer laboratory, engineering curriculum, Shepp-Logan phantom, X-ray imaging, magnetic resonance imaging

TIBBİ GÖRÜNTÜLEME SİSTEMLERİNE YÖNELİK BİLGİSAYAR LABORATUVARI DENEYLERİNİN TEK BİR NESNE İÇİN TASARLAMASI, UYGULAMASI VE DEĞERLENDİRİLMESİ

ÖZ

Elektrik ve elektronik mühendisliği (EEM) müfredatının önemli bir yönü olan tıbbi görüntüleme sistemleri (TGS), fizik, enstrümantasyon, veri toplama, görüntü üretimi, modelleme ve kalite değerlendirmesi dahil olmak üzere çok çeşitli yaklaşımları kapsar. Birçok EEM müfredatı, öğrencilere tüm çağdaş tıbbi görüntüleme sistemlerini tanıtan iyi yapılandırılmış bir TGS dersi içermesine rağmen, MIS laboratuvar çalışması görüntü işleme ile sınırlıdır.

Bu tezde, MIS ile ilgili çalışmaların uygulanabilirliğini ve anlaşılmasını artırmak için bir dizi laboratuvar deneyi tasarlanmıştır. Geleneksel X-ışını, Bilgisayarlı Tomografi (BT) ve Manyetik Rezonans Görüntüleme (MRI) modalitelerinin işleyişi, Shepp-Logan fantomu kullanılarak simüle edilir. Geleneksel biyomedikal görüntü elde etme teknikleri, farklılıklarının ve benzerliklerinin anlaşılmasını kolaylaştırmak için aynı fantom kullanılarak analiz edilmiştir. Her modalite için simülasyonlar yoluyla, görüntüleme sistemleri için uygulamalı bir öğrenme stratejisi geliştirilir.

Geliştirilen deneysel prosedürlerde, her bir özel durum için oluşturulan algoritmalar ile her bir modalitenin simülasyonu sırasında ayarlanabilir parametreler kullanılarak her görüntüleme sistemi için birden fazla durum görüntülenebilir. Akla gelebilecek tüm senaryoların simüle edilmesi amaçlanmaktadır. Elde edilen sonuçlar, görüntüleme sistemlerinin çeşitli koşullarının yanı sıra farklı modaliteleri karşılaştırma imkanı sunar. İçerik, X-ışını radyografisi ve CT için projeksiyon ve geri projeksiyondan oluşurken, k-alanı işlenir ve MRI için çeşitli rekonstrüksiyon yöntemleri analiz edilir.

Anahtar kelimeler: Bilgisayar laboratuvarı, mühendislik müfredatı, Shepp-Logan fantomu, X-ray görüntüleme, manyetik rezonans görüntüleme

CONTENTS

	Page
M. Sc THESIS EXAMINATION RESULT FORM	ii
ACKNOWLEDGEMENTS	iii
ABSTRACT	iv
ÖZ	v
LIST OF FIGURES	viii
LIST OF TABLES	xii
CHAPTER ONE – INTRODUCTION	1
1.1 Aim of the Study.....	3
1.2 Thesis Outline.....	3
CHAPTER TWO –THEORETICAL BACKGROUND.....	5
2.1 The Shepp-Logan Phantom.....	5
2.2 X-Ray.....	7
2.3 Computed Tomography.....	8
2.4 Magnetic Resonance Imaging	11
2.4.1 K-space	16
2.5 Parallel Imaging	19
2.5.1 Parallel Imaging with Localized Sensitivities (PILS)	19
2.5.2 Sensitivity Encoding (SENSE).....	21
CHAPTER THREE – MATHEMATICAL MODELS.....	24
3.1 Projection	24
3.2 Back-Projection.....	25
3.3 Concept of Parallel Imaging	27

CHAPTER FOUR – APPLICATIONS AND RESULTS.....	30
4.1 Method and Outcome of X-ray	31
4.2 Method and Outcome of CT.....	33
4.3 Method and Outcome of PILS.....	39
4.4 Method and Outcome of SENSE.....	44
CHAPTER FIVE –COMPARISON.....	55
5.1 Comparison of X-ray and CT	56
5.2 Comparison of PILS and SENSE.....	57
CHAPTER SIX – IMPLEMENTATION AND EVALUATION.....	63
CHAPTER SEVEN – CONCLUSIONS.....	69
REFERENCES.....	70

LIST OF FIGURES

	Page
Figure 2.1	The 2D Shepp-Logan phantom5
Figure 2.2	The 3D Shepp-Logan phantom.....6
Figure 2.3	Distinct applications make use of specific aspects of X-ray spectrum ..7
Figure 2.4	X-ray image of Roentgen's wife hand8
Figure 2.5	a) The first clinical CT scan axial image b) Axial CT visualization of a brain obtained using a cutting-edge CT device10
Figure 2.6	a) First brain MR image b) Advanced technology MR image12
Figure 2.7	The spin magnetization vector M extends parallel to the position of the main magnetic field B_013
Figure 2.8	The left image is an illustration of the protons randomly spinning around their axes14
Figure 2.9	The upper image is an illustration of how M_z changes after the RF excitation stops.....15
Figure 2.10	(a) The presence of raw information in k-space. (b) The related image information obtained with 2D inverse FT17
Figure 2.11	The left images (a) and (b) are fully-encoded k-space and its corresponding image in image domain.....18
Figure 2.12	PILS mechanism built with four receiver coil arrays19
Figure 2.13	The PILS mechanism21
Figure 2.14	Illustration of SENSE mechanism with acceleration factor equal four22
Figure 2.15	The unfolding mechanism of an image with an acceleration factor of two is acquired using a four-channel linear array.....23
Figure 3.1	Projection sample and imaging device elements24
Figure 3.2	An example of chest X-ray25
Figure 3.3	The exhibit of projections taken from various angles26
Figure 3.4	Illustration of the back-projection concept26
Figure 3.5	Placement of a Coil array placement for PILS27
Figure 3.6	Systems of SENSE28
Figure 3.7	Placement of a coil array29
Figure 4.1	Axial section of 3D SL phantom.....30

Figure 4.2	3D SL phantom on Matlab	30
Figure 4.3	The attenuation coefficient maps of 2D phantom.....	31
Figure 4.4	Projection of 2D SL phantom.....	32
Figure 4.5	Projection for 2D SL phantom	32
Figure 4.6	Sinogram for 2D SL phantom	33
Figure 4.7	Final image of back-projection method for 2D sample.....	34
Figure 4.8	Ram-Lak filter.....	35
Figure 4.9	Final image of filtered back-projection method for 2D sample	35
Figure 4.8	Sinogram for 2D SL phantom.....	34
Figure 4.9	Final output of back-projection method for 3D sample.....	35
Figure 4.10	Sinogram for 3D SL phantom.....	36
Figure 4.11	Final output of back-projection method for 3D sample.....	36
Figure 4.12	The final output of the reconstruction method view as slice plane for the 3D phantom.....	37
Figure 4.13	120th axial section of back-projection method result	38
Figure 4.14	The 2D high pass filter.....	38
Figure 4.15	120th axial section of back-projection method result.....	38
Figure 4.16	Gaussian sensitivity maps corresponding each receiver coil	40
Figure 4.17	Sensitivity map for each receiver coil	41
Figure 4.18	The correct subimage for each receiver coil	41
Figure 4.19	Each receiver coil's fully sampled k-space	42
Figure 4.20	Each receiver coil's under-sampled k-space, black lines represent zero-filled lines in the matrix	42
Figure 4.21	Each coil has reduced FOV image in the form of periodic repetition ..	43
Figure 4.22	The correct subimages that are extracted from periodically repetitive images of each coil	43
Figure 4.23	The final composite image acquired with PILS algorithm	44
Figure 4.24	a) Default outcome image for simulator b) k-space of outcome image for simulator	45
Figure 4.25	a) Error map for default coil radius which is 0.07 m b) Error map for coil radius equal 0.01 m c) Error map for coil radius equal 0.13 m	46

Figure 4.26	a) Error map for default distance from the coils centers to the origin which is 0.17 b) Error map for distance from the coils centers to the origin equal 0.12 c) Error map for distance from the coils centers to the origin 0.22.....	47
Figure 4.27	a) k-space created by four coils b) k-space created by eight coils c) k-space created by sixteen coils.....	48
Figure 4.28	a) Image created by four coils b) Image created by eight coils c) Image created by sixteen coils	49
Figure 4.29	a) k-space when the acceleration factor is one b) k-space when the created acceleration factor is two c) k-space when acceleration factor is four	49
Figure 4.30	a) Image when the acceleration factor is one b) Image when the acceleration factor is two c)Image when acceleration factor is four ..	50
Figure 4.31	Four-receiver coil sensitivity maps (a) represents coil 1, (b) represents coil 2, (c) represents coil 3, and (d) represents coil 4	51
Figure 4.32	Images acquire for each receiver coil with in array; (a) represents coil 1, (b) represents coil 2, (c) represents coil 3, and (d) represents coil 4..	51
Figure 4.33	Each receiver coil's fully sampled k-space data represented by 256x256; (a) represents coil 1, (b) represents coil 2, (c) represents coil 3, and (d) represents coil 4	52
Figure 4.34	Each receiver coil's undersampled k-space data represented by 256x256; (a) represents coil 1, (b) represents coil 2, (c) represents coil 3, and (d) represents coil 4	52
Figure 4.35	Reduced FOV aliased images obtained with acceleration factor equal 2; (a) represents coil 1, (b) represents coil 2, (c) represents coil 3, and (d) represents coil 4	53
Figure 4.36	Final composite image reconstructed via SENSE with 4 receiver coils and acceleration factor equal 2.....	51
Figure 5.1	X-ray result of 3D SL Phantom.....	56
Figure 5.2	Axial section CT result of 3D SL Phantom	57

Figure 5.3	Sensitivity maps of each coil acquired with standard deviation equal to a)30 c) 35 e)40 40 g)45, The PILS reconstructions for standard deviation equal b)30 d) 35 f) 40 h) 45.....	58
Figure 5.4	The image reconstructed by SENSE had an unfolding problem when the number of coils is four and the acceleration factor is five	60
Figure 5.5	The image reconstructed by SENSE had a contrast problem when the number of coils is eight and the acceleration factor is five	61
Figure 5.6	The image reconstructed by SENSE had no problem when the number of coils is sixteen and the acceleration factor is four.....	61
Figure 6.1	The graph of mean and standard deviation for the pre-laboratory assessment and post-laboratory assessment for each experiment. The lines shown represent the standard deviation, the circles represent the pre-laboratory evaluation mean, and the crosses represent the post-laboratory mean for each experiment.....	67

LIST OF TABLES

	Page
Table 2.1 The x-ray attenuation coefficient values for various tissue in different energy level	11
Table 2.2 Some type of tissues within a human body and the corresponding time constants including T1 and T2.....	16
Table 5.1 The SENSE algorithm's reconstruction outcomes; "A" stands for "accomplished," "CP" stands for "contrast problem ," and "F" stands for "failed in the unfolding process in reconstruction."	59
Table 6.1 Syllabus of designed laboratory	63
Table 6.2 Objectives of each experiment in designed laboratory	64
Table 6.3 Results of pre-laboratory and post-laboratory evaluation exams.....	66

CHAPTER ONE

INTRODUCTION

MIS are quite complicated machines that include components from almost every branch of EEE. MIS courses encompass a variety of modalities, including conventional X-ray imaging, Computed Tomography (CT), and Magnetic Resonance Imaging (MRI) and others (Haidekker, 2013). Beginning with the fundamental physical concepts underlying these imaging systems, data collection, image formation, equipment, and quality aspects are analyzed (Prince & Links, 2006; Zho et al., 1993).

The conventional lecture format prevents students from developing practical abilities in relation to operational and emerging challenges in MIS, which need considerable background knowledge. Thus, more laboratory experiments are required to provide a complete understanding (Kaçar & Bayilmis, 2013; Stanley et al., 2004). Unfortunately, these modalities are only available in hospitals and research institutions. Computer studies are used to solve this limitation, however, they are mostly focused on image processing (Dikshit et al., 2005) and evaluation (Sonka et al., 1998). In this thesis, a two-dimensional (2D) and three-dimensional (3D) experiment-based course were built, with the same example used in certain modalities to enhance learning efficiency. Students are asked to evaluate the findings obtained by generating a sample of varying parameters (Alexiadis & Mitianoudis, 2013; Glatard et al., 2013; Wilhjelm et al., 2008).

The conventional laboratory contains a set of computer exercises and their configuration in accordance with the EEE curriculum to supplement theoretical MIS lectures and aid in the comprehension of ideas covered in undergraduate MIS courses. The desired objective is for each experiment to concentrate on a different area of the MIS and to allow the application of information obtained in various EEE courses. While it is possible to understand the MIS subject and gain practically, it is also important to emphasize the relevance of various EEE disciplines.

The general design conditions to achieve these goals are mainly as follows: Each experiment should design to concentrate on the “difficult-to-comprehend” aspect(s) of the imaging system. Each experiment ought to include a concept that focuses on a critical also thriving aspect of the imaging system. Each experiment should focus on a different aspect of MIS (for example, fundamental physics, image production, equipment, quality standards, and so on) to illustrate the significance of each component. Each experiment should allow for the application of information and skills obtained in EEE courses. Each experiment should involve a distinct aspect of background knowledge, such that the entire set of experiments encompasses a broad variety of EEE curriculum topics (Paschal et al., 2006).

While the proposed schedule has been proven to be instructional and motivating, it has been shown to have limitations in reality. Each experiment has a distinct and specific purpose, which the student should understand before beginning the lab study. This technique has been observed to have two downsides. The first drawback is that comparisons across modalities are restricted since each experiment has a distinct objective. Second, it may be quite difficult for students to comprehend the essence of the experiments, particularly at the semester's conclusion. The students conclude that the precise aims of each experiment make obtaining extra resources for study very challenging. Taking these drawbacks of the existing lab schedule into account, new design criteria are established to improve MIS understanding. As a result, three New Design Criteria (NDC) have been established to accomplish these objectives:

NDC-1) All imaging experiments should be performed on the same subject such that the students can learn the properties of the object to be imaged just once at the beginning of the semester. There should be both 2D and 3D models together with analytical representations of the same object in Cartesian (i.e. image) and frequency (i.e. Fourier) domains(if possible).

NDC-2) The subject should have varying properties that would cause alterations on the acquired images such that students have the possibility to compare the results of different experiments and can make direct observations on the advantages and

disadvantages of a selected modality.

NDC-3) The content of the experiment should allow student to search the material directly.

Those new design criteria can be considered as additional design criteria for the previously proposed laboratory curriculum (Selver, 2015). In spite of fact that the laboratory will have the same purpose, these new design criteria will help the students to understand the fundamentals and the differences of various medical imaging modalities more easily.

1.1 Aim of the Study

This thesis aims to design a set computer laboratory experiments, which uses a single object for all modalities such that the students can observe the differences between acquired and/or reconstructed images. This would help the students to understand and compare various imaging technologies by comparing their characteristics on the same target. This can be accomplished in 2D and 3D for all imaging systems by constructing a phantom, the physical properties (i.e. x-ray absorption coefficient, gyromagnetic ratio(s) of the inner structures etc.) of which is determined in detail. Since all of the experiments will be carried out on the same phantom, the outcomes will be straightforward to compare. As a result, the students will be able to examine the unique characteristics of each imaging system. The outcomes can be produced and observed with controllable parameters for many distinct circumstances. A more effective learning process will be achieved by using a step-by-step reconstruction of all modalities, the theory of which have been previously learned.

1.2 Thesis Outline

Six chapters are included in this thesis. Chapter One provides an introduction to essential information regarding MIS. The background information for each modality,

(i.e. X-ray, CT, and MRI), and also SL phantom is given in Chapter Two. The information on the x-ray projection, CT back-projection, and parallel imaging concepts are covered in Chapter Three. Chapter Four shows the outcomes of all processes for X-ray and CT using 2D and 3D examples. Furthermore, the impacts of numerous factors were analyzed using an MRI simulator, and reconstruction approaches were done step by step, with all outcomes provided. First, data acquired from X-rays and CT are compared, and then the MRI methods are compared in Chapter Five. Chapter Six covers implementation of the laboratory and the evaluation of the whole laboratory. Chapter Seven covers consequences for the whole research.



CHAPTER TWO

THEORETICAL BACKGROUND

In this section, the SL phantom used to simulate each imaging system will be described. Following an overview of the emergence of X-ray and CT imaging systems, fundamental information regarding both imaging systems is discussed. Additionally, the principles of MRI are described step by step. Then, the terms k-space and image space for MRI are defined and compared. The MRI reconstruction methods PILS and SENSE are defined, and information on each is provided.

2.1 The Shepp-Logan Phantom

In 1974, the SL phantom was created as a tool to simulate image reconstruction (Shepp et al., 1974). To simulate the head, the model utilized ten ellipses of various sizes and densities. An optional 11th ellipse can be used to depict brain hemorrhage inside the skull to test image reconstruction. In general, phantoms with a size of 256x256 can be used in both 2D and 3D.



Figure 2.1 The 2D Shepp-Logan phantom (Gach et al. 2008)

A 2D SL phantom with a size of 256x256 is shown in Figure 2.1. It is composed of ten ellipses in different positions of varying densities. The 3D SL phantom is shown in Figure 2.2. No ellipses intersect in the 3D phantom. Due to the fact that the 2D phantom is like a slice of the 3D phantom, several ellipses in the 2D phantom intersect.

Reconstruction algorithms must be analyzed and validated. Typically, the first stage - numerical evaluation - is based on synthetic data experiments (Guerquin-Kern et al., 2010). The other stage is generally calculated from a mathematically determined phantom that provides the reconstruction's reference data. The SL phantom, which was first suggested for CT, is a commonly available candidate.



Figure 2.2 The 3D Shepp-Logan phantom (Cheng et al. 2007)

Due to its versatility, the SL phantom has been used in a broad range of imaging modalities. The phantom's adaptability placed it in a very beneficial area since it can be adjusted and modified as needed. The phantom's usefulness has improved due to the flexibility of changing the number of ellipses, densities, and ellipse locations. The main factors for utilizing SL phantom are reducing costs associated with obtaining valid scanner data, also assessing the reconstruction software's output, and having accurate ground-truth data to analyze (Guerquin-Kern et al., 2012).

The phantom designed by Shepp and Logan for tomography was later used for MRI as well. In 1997, Smith et al. conducted the first experiment using the SL phantom in the area of MRI (M. R. Smith et al., 1997). Smith et al. emphasizes the significance of precise simulations for the analytical confirmation of MR reconstructions. Afterward, Walle et al. identified the SL phantom's quantitative Fourier expression as a series of ellipses (Walle et al., 2000). Cheng et al. suggested a 3D adaptation of a SL phantom for MRI (Cheng et al., 2007). Lastly, Gach et al. reviewed and concluded these studies by suggesting specific spin density parameters and considering the impact of T1 & T2 relaxation times in order to represent much more realistic data (Gach et al., 2008).

2.2 X-Ray

The electromagnetic spectrum is a description and classification of electromagnetic waves based on their varying wavelengths. X-rays including visible light, ultraviolet light, infrared light, gamma rays, and microwaves, are forms of electromagnetic radiation. Medical imaging is amongst the most popular and useful applications of X-rays. X-rays are used to diagnose and treat cancer, as well as to explore the environment.

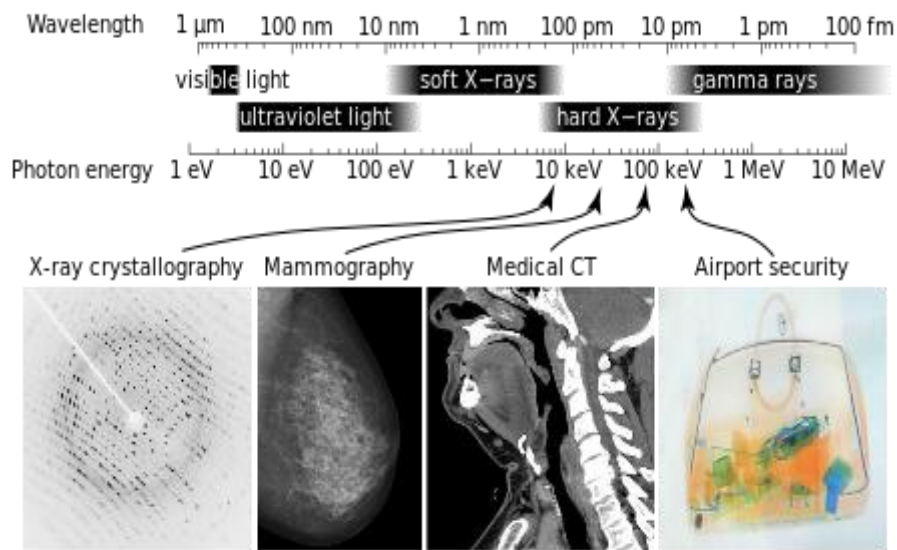


Figure 2.3 Distinct applications make use of specific aspects of a X-ray spectrum (Veena. T, D. V. Chidanand, 2015)

X-rays are divided into two main categories: soft and hard X-rays (Veena. T, D. V. Chidanand, 2015). Soft X-rays are in the electromagnetic spectrum range between gamma radiation and ultraviolet light. Soft X-rays have higher frequencies and shorter wavelengths. The electromagnetic spectrum region occupied by gamma radiation and hard X-rays is the same. The major difference is that X-rays were often produced by speeding electrons, whereas gamma-rays were produced by nucleons.

In 1895, the finding of X-rays marked the start of a shift in our view of the physical universe. Wilhelm Conrad Roentgen, a researcher at Wurzburg University, discovered X-rays in 1895 (Assumus, 1995). To emphasize the novel essence of his findings, he

coined the term x-rays, though they have been now known to as Röntgen-rays. In the same year, Röntgen's wife had first x-ray image taken of her finger bones and ring, which was captured on film (Mikla et al., 2012).



Figure 2.4 X-ray image of Roentgen's wife hand (Mikla et al. 2012)

X-rays, which are electromagnetic waves, function similarly to light rays but with slightly shorter wavelengths and can penetrate some thicknesses of matter (Seyyedi, 2018). X-ray imaging processes are widely utilized for the safe characterization and analysis of a vast variety of objects in 2D and 3D. Due to X-rays' ability to penetrate deeply into material, they are an excellent instrument for visualizing an object's internal morphology (Mohan et al., 2020).

X-ray imaging is the first type of internal medical imaging and has long been radiology's mainstay. X-ray imaging examinations are also the most widely used diagnostic imaging techniques currently. The key benefits of x-ray imaging are its simplicity and high image quality for a wide range of diagnostic techniques, as well as its short scanning times and relatively low expenses (Ahmad et al., 2014).

2.3 Computed Tomography

CT is a non-invasive method for visualizing internal characteristics of solid structures and collecting digital data on their 3D geometries and properties. It provides specialists with a more precise view of the human body and enables the secure, simple, and quantitative localization of lesions, and other conditions that would be painful,

hazardous, or perhaps even impossible to detect using other techniques (Shepp & Kruskal, 1978).

Although CT became practical with the advent of new computing technology in the 1960s, some of the concepts that underlying it based the beginning of the twentieth century. Johann Radon demonstrated that if integral values of any number of lines moving through an object layer are established, the distribution of that substance or material property can be determined in 1917 (Kalender, 2006).

The first studies on reconstructive tomography's medical applications were conducted by physicist A M Cormack in 1963, when he established a system for measuring the radiation absorption distribution throughout the human body using transmission measurements (Cormack, 1964). Godfrey Hounsfield, a British engineer widely known as the creator of computational tomography, conducted the theory's first successful practical demonstration in 1972 (Hounsfield, 1973). Cormack and Hounsfield were jointly awarded the Nobel Prize in Medicine for their extraordinary achievements in 1979.

CT is a well-established x-ray imaging modality with a broad range of applications ranging from medical imaging to industrial non-destructive inspection. The first of the innovative slice-imaging modalities, X-ray CT scans, was introduced into clinical research in 1972 (Kalender, 2006). Initially, devices used only for head imaging were available, but "whole body" systems with wider patient openings were introduced in 1976. CT has become widely accessible around 1980 (Hounsfield, 1980).

The first CT scanner was implemented at Atkinson Morley's Hospital in 1971, and the first patient scanned was a middle-aged woman with a possible frontal lobe tumor shown in Figure 2.5.a (Beckmann, 2006). An axial CT image of the brain acquired with a state-of-the-art CT device, a 512 x 512 matrix image is shown in Figure 2.5.b.

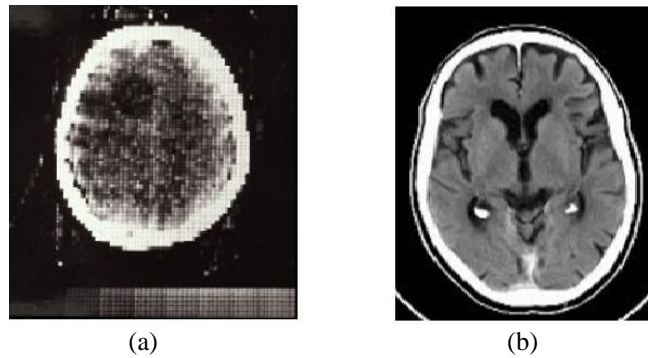


Figure 2.5 a) The first clinical CT scan axial image (Beckmann, 2006) b) Axial CT visualization of a brain obtained using a cutting-edge CT device

A CT scanner utilizes a sequence of 2D x-ray projections from various angles and employs computer technology to produce a 3D image, or slice, of a clinical sample such as organs, blood vessels, bones, or some industrial products (Seyyedi, 2018). If you take several x-rays of the same region from various angles, a computer can combine the data from the x-rays to produce a cross-sectional image. CT scanning utilizes data collected from an X-ray tube spinning around the patient to create cross-sections of the body.

CT is especially crucial as a consequence of its vastly enhanced image quality over prior x-ray projection imaging and its capability to provide image volumetric details across the x-ray imaging methods (Ahmad et al., 2014). CT imaging has made significant advancements in terms of speed, client experience, and resolution. More anatomy can be scanned in less time after advances in CT scanning technology. Rapid scanning assists with removing artifacts associated with patient motion, such as ventilation or gastric motility. Significant study and development have been conducted to achieve the highest image quality available for the minimum possible x-ray dose (Villarraga-Gómez et al., 2019).

Pursuing Wilhelm Röntgen's discovery of X radiation, it was soon applied to the field of tomography. Tomographic imaging is the process of focusing X-rays towards an object from various angles and calculating the strength decrease over a sequence of linear paths (Wang, 2017). Beer's Law which is its shortest form shown in Equation

2.1 defines this decrease in strength as a function of X-ray power, route length, and substance linear attenuation coefficient.

$$I = I_0 \cdot e^{-\mu d} \quad (2.1)$$

where I_0 and I are the original and final X-ray intensities, respectively, μ is the linear attenuation coefficient of the material, and d is the X-ray path length.

Table 2.1 The x-ray attenuation coefficient values for various tissue in different energy level (Tekin et al., 2017)

Tissue	60 keV	80 keV	150 keV
Bone	0.3148	0.2229	0.1480
Brain	0.2058	0.1831	0.1498
Fat	0.1974	0.1800	0.1500
Blood	0.2057	0.1827	0.1492
Muscle	0.2048	0.1823	0.1492
Lung	0.2053	0.1826	0.1493

2.4 Magnetic Resonance Imaging

MRI is a relatively recent method and has been in existence since the early 1980s. MRI is a safe and effective medical test used by physicians to detect medical problems. It produces accurate images of muscles, soft tissues, bone, and almost all other body's internal structures using a strong magnetic force radio frequency signals, and a computer (Chan et al., 2018).

The name known as MRI comes from NMR due to the publication of a special technique that creates 2D images obtained with NMR signals, in 1973. After this, MRI has always followed a developmental path since it was promised as an advantageous imaging technique in clinical applications. MRI has the ability to produce images of human body in the form of slices and cross-sections. These images especially include information about soft tissues within the body (Ledoux et al., 2019). For this reason, MRI has been taking an effective role in clinical applications for diagnosis purposes.

An MRI device employs a powerful magnet, RF coils, and gradient coils to detect signals in the radio frequency range of the electromagnetic spectrum (Chan et al., 2018). Protons, in other words hydrogen atoms, are used to acquire MR signals during an imaging procedure. Since the human body is a rich source of water molecules consisting of two hydrogens and one oxygen atom, plenty of hydrogen within the human body allows their usage in MR imaging (Cooper, 2000; Konez, 1995).

MRI does not utilize ionizing radiation. This guarantees that no X-rays or other harmful types of radiation are being used. MRI systems differ from other imaging technique at this point as it utilizes magnetic fields, to create the desired image, which has no harm for human body detected so far.

Doctors may use detailed MR images to examine different sections of the body to ascertain the prevalence of specific diseases. The images may be viewed on a screen display, electronically transmitted, scanned or transferred to a CD, or submitted to a digital cloud service. The images provided by an MRI scan are significantly accurate and therefore have decent diagnostic quality. MRI technology is developed day by day. Figure 2.6 show improvement of MRI technology last 30 years.

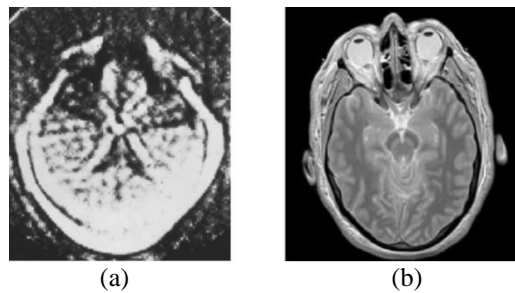


Figure 2.6 a)First brain MR image b) Advanced technology MR image (Kumar, 2014)

In 1967, Nottingham University Hospital employed MRI for the first time clinically. Sir Peter Mansfield, 2003 Medical Nobel Prize winner, pioneered research that allowed NMR to be used as a diagnostic imaging modality (Boesch, 2004). At the time, the images were low quality and thus unsuitable for professional use. Paul Lauterbur from Stony Brook applied magnetic field gradients in all three dimensions and computerized axial tomography projection to create NMR image (Lauterbur, 1973).

The technique utilizes a special rotational movement called “spin” of the atoms which have odd numbers of proton or neutron, such as hydrogen (Alg & Atalar, 2015). The spin phenomenon is considered advantageous in order to obtain the MR signal that effectuates the eventual image of the desired location.

An MRI scanner basically, makes use of a strong magnetic field created by a big main magnet. Matters, which are placed within this magnetic field, interact with it in various ways (Kharzeev et al., 2012). In the case of MRI, the hydrogen atoms are the point of interest due to their abundance in tissues like water and fat within the whole body (Berger, 2002). A hydrogen is an atom consisting of a proton and an electron. Since it has only one proton, it is able to process the spin movement which is a phenomenon covered and explained by the quantum mechanics (Alg & Atalar, 2015). In literature, protons are considered as a gyroscope due to this spin movement that is a rotational movement on an axis, with a north-south pole (Berger, 2002).

Majority of a human body, 60-80%, consists of water molecules, known as H_2O (Cooper, 2000). Since the water is a rich source for hydrogen atoms, it becomes an important focus for MRI. The hydrogen atoms, standing for protons, are randomly aligned and spin in human body with respect to the earth’s magnetic field under normal conditions. Because of this movement with two different poles, each individual proton act like a small bar of magnet that each can be named as a dipole. However, the net magnetization created by this hydrogen population is always zero as the magnetization vectors of hydrogens cancel out each other. Hence the body, as whole, does not exert any magnetic effect.

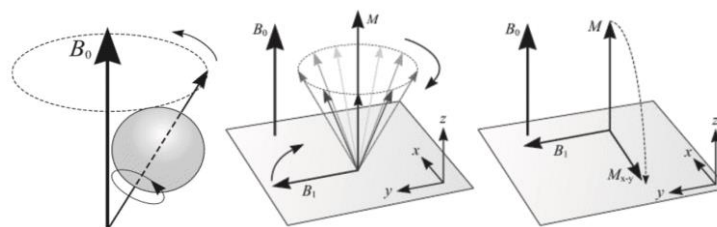


Figure 2.7 The spin magnetization vector M extends parallel to the position of the main magnetic field B_0 . If an RF wave in the “y” direction having the same Larmour frequency applies to the spin, it tilts M in the “x” direction towards the horizontal plane. M_{xy} is the horizontal plane’s corresponding part of M , and it is referred to as transverse magnetization (Alg & Atalar, 2015)

The axis of rotation of the hydrogen atoms (protons) are aligned with the magnetic field vector because the main magnetic field called " B_0 " forces the hydrogen atoms to change their axis of rotation in the same direction, which is in z-direction. This is due to the fact that most of the individual magnetization vectors of the protons are aligned parallel with the main magnetic field vector, the net magnetization vector (M) created by the rotations of the protons, the main magnetic field vector.

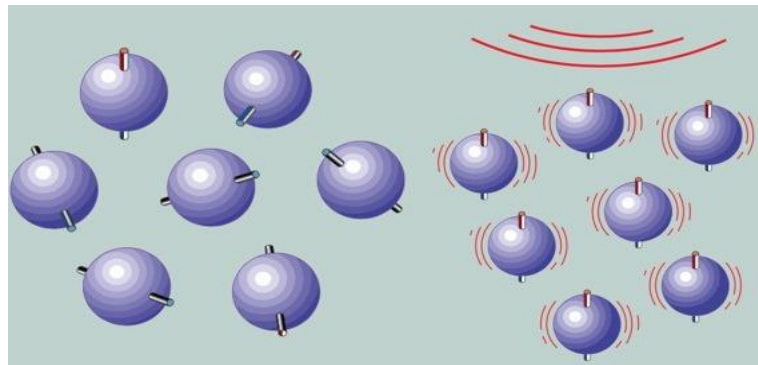


Figure 2.8 The left image is an illustration of the protons randomly spinning around their axes. The right image shows the protons' axes aligned uniform with respect to the external magnetic field shown by three big red arcs (Berger, 2002)

The spin motion of hydrogen atoms takes place at a special frequency called the "Larmour Frequency" that changes depending on the size of the magnetic field and their gyromagnetic values (Alg & Atalar, 2015). If an additional magnetic field " B_1 ", known as a radiofrequency (RF) wave and is in the same frequency as the larmour frequency, hydrogen atoms spin axes are tilted to a different plane, which is named as "transverse plane" or "xy-plane". This situation is called "excitation" and explained with the resonance phenomenon, and is a beneficial process in MRI. As a result, the spinning protons' net magnetization vector " M " is perpendicular to B_0 , and this magnetization vector is referred to as "transverse magnetization" (M_{xy}). The tilt angle is referred to as the "flip angle," and the deflection angle is proportional to the amplitude of the B_1 .

After the B_1 magnetic field is removed from the environment, the spins stimulated by the RF waves begin to return to their original position, which is parallel to the main

magnetic field B_0 . This is since the main magnetic field forces the magnetization vector M in the same direction as the main magnetic field. Due to the fact that the orientation of the magnetization vector M varies in the presence or absence of RF waves, it can be divided into two parts denoted by M_z and M_{xy} to improve analysis. While M_z , which is zeroed immediately after the end of B_1 stimulation, begins to increase in the z -direction, M_{xy} begins to decrease over time, this is referred to as "relaxation" (Alg & Atalar, 2015).

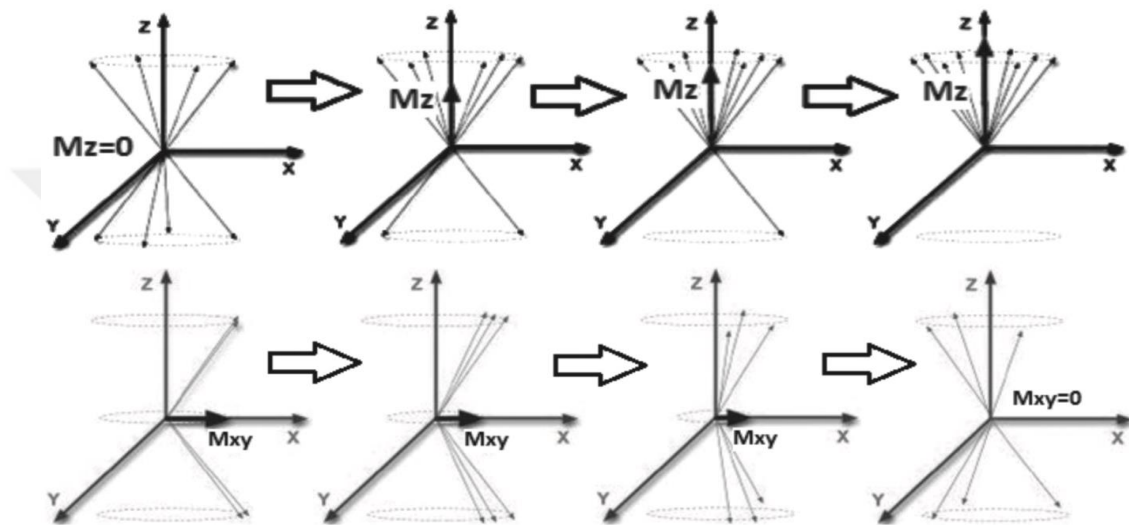


Figure 2.9 The upper image is an illustration of how M_z changes after the RF excitation stops. The bottom is the illustration of M_{xy} for the same condition. When the 90° RF pulse stops, M_z starts increasing while M_{xy} decreases at the same time (Alg & Atalar, 2015)

The relaxation process, the change of the magnetization vector from the xy -plane to the z direction, occurs at a certain time. This particular time creates contrast mechanisms between tissues as it is different for each tissue. MR signals, that contribute to the final image formation, are acquired during relaxation processes. The change in magnitude of the magnetization vectors on both xy -plane and z -direction create signals in receiver coils. These signals are obtained and stored as raw data which will then be processed.

When the magnetic field B_1 is removed from the system, the magnetization vector on the xy -plane starts decreasing and it creates MR signals on the receiver coils. This type of signal receiving is also named T_2 relaxation. The time constant " T_1 ", which is

the time it takes from the initial magnitude of the magnetization vector to a 37% reduction. T_1 relaxation takes longer than T_2 . In addition, while T_1 duration increases with the magnitude of the main magnetic field B_0 , T_2 is independent of it.

Table 2.2 Some type of tissues within a human body and the corresponding time constants including T_1 and T_2 (Alg & Atalar, 2015)

Tissue	T_1 (ms)	T_2 (ms)
White Matter	780	90
Grey Matter	920	100
Fat Tissue	240-250	60-80
Muscle Tissue	860-900	50

Table 2.2 encapsulates information about relaxation constants of various tissues in the human body that have been evaluated and published in the literature (Bottomley et al., 1984; Stanisz et al., 2005). The knowledge of these different time constants provides the ability to distinguish among various tissues in the same MR image. For a specific instance of a T_1 -weighted image that contains both white matter and fat tissues; discrimination between these two types of tissues is a possible task to do because of the T_1 duration difference between white matter and fat tissue.

2.4.1 K-Space

K-space is a matrix of numbers that represents the spatial frequencies within MRI. The prevalent portrayal of k-space as a "galaxy" sustains the mystery. Each k-space "star" is simply a data point extracted directly via the MR signal. The brightness within each star demonstrates the star's specific spatial frequency's relative contribution to the final image (Sykora et al., 2010).

Receiver coils detect MR signals and store them as raw data with a matrix called the k-space matrix. K-space has two dimensions, k_x and k_y , which correspond to axes.

The k-space includes details about the object's frequency and amplitude at various phases. The inverse Fourier transform (FT) of the raw data in the k-space is taken to obtain the spatial information of the object (Alg & Atalar, 2015).

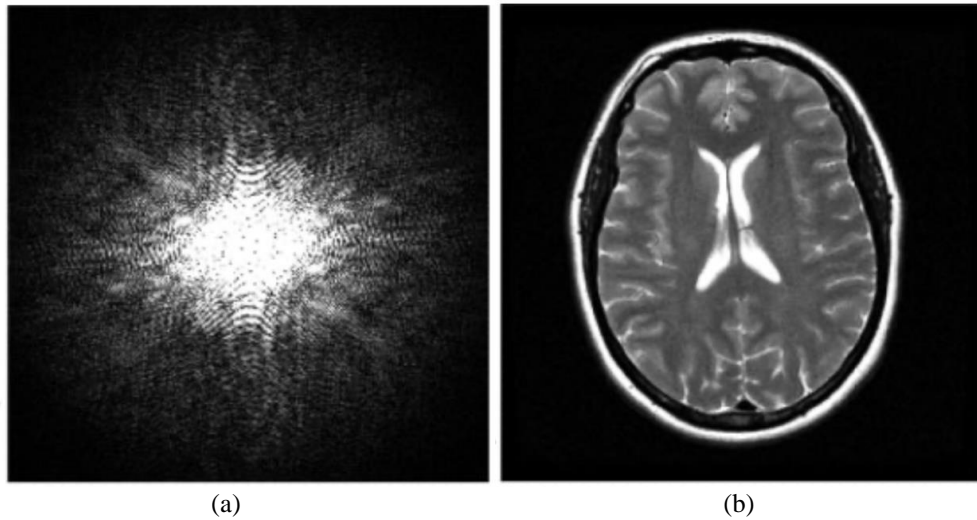


Figure 2.10 (a) The presence of raw information in k-space. (b) The related image information obtained with 2D inverse FT (Paschal & Morris, 2004)

To get a deeper understanding of k-space, it is essential to reconcile frequency and object spaces. In the object space, a rapid change means high frequency, while a slow change such as a flat region refers to low frequency. The data points in the middle of the k-space have a low frequency and contain information corresponding to slow changes in the object being imaged. On the other hand, data at the points far from the k-space central have high frequencies and contain the information of rapid changes in the object, complying with fine details (Alg & Atalar, 2015).

The resolution of the images obtained with MRI is important in terms of both radiological and computer evaluations. The spatial resolution, about the k-space, is proportional to the gradients' magnitudes and their duration of application. Associated with the FT relation, the resolution of an MR image is associated in the furthest points in k-space, in both x-direction and y-direction.

Low frequency information is responsible for the bulk image and contrast, while higher frequencies refer to the sharp transitions and details. In Figure 2.11, a set of k-

space matrices and their corresponding images are shown. The first k-space is fully-encoded, the second one is the lower (central) frequencies deleted version, while the last one is higher frequencies deleted version. They are shown as “a”, “c”, and “e”.

The image, obtained with 2D inverse FT of the full k-space, has full resolution and contains all available information. The second image is obtained by using higher frequencies, lacking of low frequency information. It is noticeable that the image is easy to perceive due to the sharp transitions. However, it suffers from contrast because the lower frequency information is not contributed to the image formation. These properties of k-space have become the intriguing points for the parallel imaging. It is because some potential disadvantageous properties of k-space turned out to advantages by utilizing parallel imaging modalities to acquire an MR image.

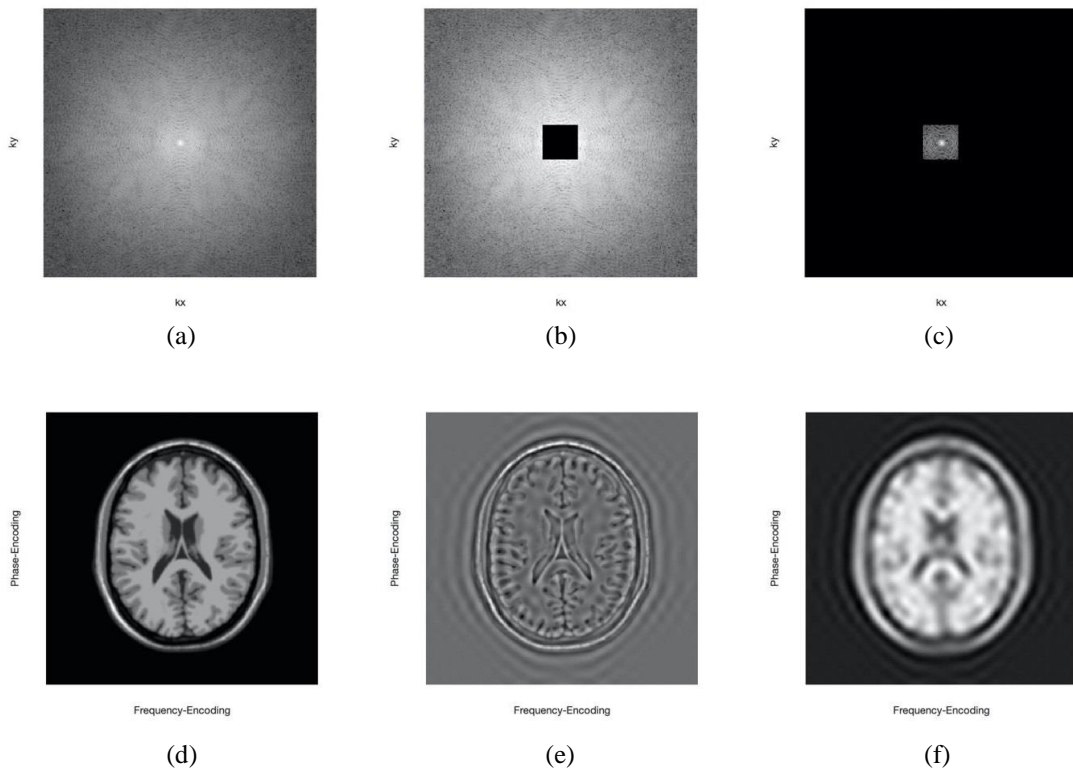


Figure 2.11 The left images (a) and (b) are fully-encoded k-space and its corresponding image in image domain. The middle images (c) and (d) are the k-space with no low frequency information and the corresponding image having recognizable sharp edges but low contrast. The right images (e) and (f) are the k-space lacking of high frequency information and the corresponding image that are blurry and less detailed

2.5 Parallel Imaging

Imaging speed and total duration of data acquiring in MRI are considered as the most momentous topics especially in clinical experiments of MRI (Blaimer et al., 2004). Parallel imaging was developed to expand the abilities of MRI beyond its technological and physiological limitations. Although a traditional MRI system obtains information by quickly swapping magnetic field gradients open and close, this imposes a limit on the scanning rate. Parallel imaging is an advantageous option in this situation since it enables the processing phase to be accelerated by using a variety of image restoration approaches.

Parallel MRI allows use of an array of receiver coils. It is rooted in the synchronized acquisition of MR signals from numerous receiver coils in a particular area with a defined spatial sensitivity map (Pruessmann, 2006). All receiver coil in the arrays receive information from the area defined by its own sensitivity, and the images acquired by each coil are then integrated with information about the coil sensitivities to produce a final image (Alg & Atalar, 2015). Due to the time and technological constraints associated with acquiring a completely encoded k-space, parallel imaging enables the creation of an MR image from just a subsampled k-space, thus speeding up the MRI process.

2.5.1 Parallel Imaging with Localized Sensitivities

The assumption underlying Parallel Imaging with Localized Sensitivities (PILS) is that each single-coil in the array has a localized sensitivity map, indicating that their

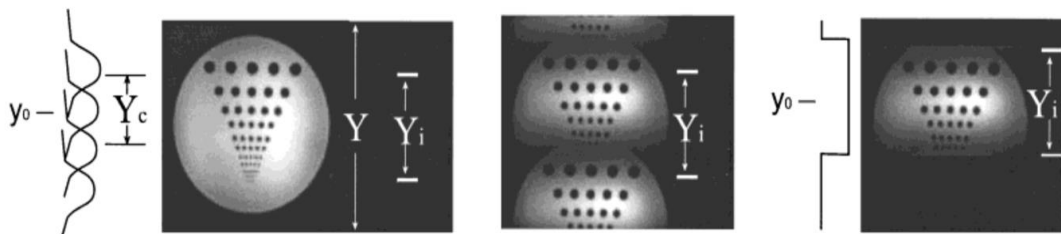


Figure 2.12 PILS mechanism built with four receiver coil arrays (Griswold et al, 2000)

sensitivity is limited to a narrow area (Griswold et al., 2000). PILS is one of the MRI methods that relies on the image domain to reconstruct a composite image obtained with the k-space from each receiver coil.

The basic concept of PILS is to generate reduced field of view (FOV) images of the receiver coils from the receiver coil sensitivity maps used as filters, and then to obtain the composite reconstructed image using those images. Each receiver coil's sensitive area is denoted by Y_c , and its center is denoted by y_0 . Every receiver coil has a different center, and their spatial positions correspond to the areas in the reference image. It makes the coils responsible for the different parts within the full FOV image (Blaimer et al., 2004).

The four-receiver coils array for the PILS technique is shown in Figure 2.12. In image "b," aliased and repeated images are shown in the complete region of interest, while image "c" shows the presence of the right sub-image separately. The primary process of PILS is to generate a Y_i image for each receiver coil. For the receiver coil set, this process results in aliasing images after acquiring less k-field data matrix. As far as the " $Y_c < Y_i < Y$ " requirement is followed, aliased images are totally distinct from full FOV images (Blaimer et al., 2004).

Periodically repeating the sub-images using the spatial location of each receiver coil. Using the sensitivity map information of the coils in the array set, accurate sub-images are extracted from the images of each receiver coil. Each receiver coil acts as an analog filter, allowing the acquisition process to be carried out (Griswold et al., 2000). Due to this reason, proper sub-images are processed separately, while periodical repeats of full FOV images are suppressed. The full FOV image is obtained from all receiver coil in the array. The proper sub-images of each receiver coil are then merged to get the final composite image at the end of the procedure.

The PILS mechanism must be determined by the appropriate positioning of the receiver coils as an array set (Blaimer et al., 2004). This is because the sensitivity maps of each coil can overlap, which can adversely affect the overall image quality due to

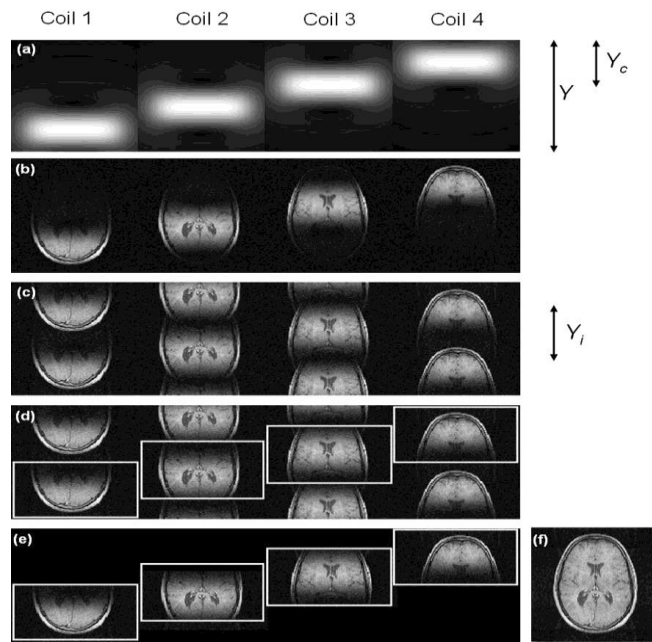


Figure 2.13 The PILS mechanism; (a) 4 receiver coils arranged in phase-encoding direction, (b) images obtained with each receiver coil, (c) reduced FOV Y_i images, (d) extraction of correct subimages, (e) using receiver coils as analog filters, (f) reconstruction of the correct subimages in a composite image (Blaimer et al., 2004)

the mutual inductance problem between the receiver coils (Roemer et al., 1990). This may be avoided by ensuring zero or low interaction among the receiver coils. Another limitation of PILS is related to the ratio between the acceleration factor and the number of receiver coils. Acceleration factors of about half the amount of receiver coils in the series are convenient for achieving the highest possible signal to noise ratio (Griswold et al., 2000). SENSE is the other parallel MRI method that works on the image domain to reconstruct the final image from aliased receiver coil images. It is referred to as an "unfolding" mechanism, related to the processes of unfolding the images that have been folded over one another.

2.5.1 Sensitivity Encoding

SENSE is the other parallel MRI method that works on the image domain to create a composite image from aliased receiver coil images. It is referred to as an "unfolding" mechanism, related to the processes of unfolding the images that have been folded

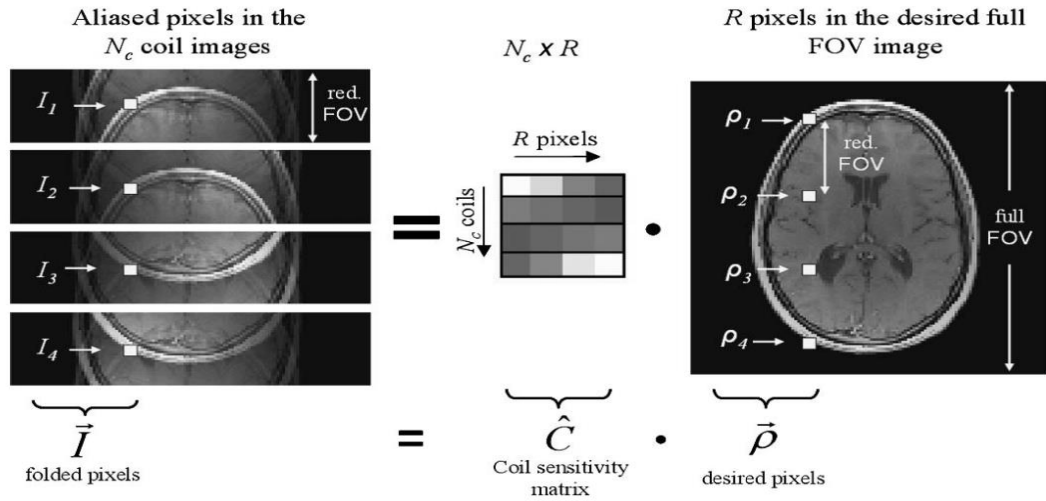


Figure 2.14 Illustration of SENSE mechanism with the acceleration factor $R=4$ (Blaimer et al., 2004) over one another (Blaimer et al., 2004). Folded images, often referred to as aliased images, are the products of rapid k-space data acquisition. It causes reduced FOV images generated by the receiver coil when the number of information-filled lines in the K-space decreases. Depending on how many pixels are overlapped, the unfolding process for pixels in images can be performed using a reduced FOV.

The SENSE parallel MRI algorithm begins by generating sensitivity maps for each receiver coil. Because of the various placement of the receiver coils that can be achieved, the sensitivity maps for each receiver coils must be exactly created. Due to the reduced k-space data, pixels at a particular location may overlap each other. An unfolding process is performed for all overlapped pixel, using the sensitivity map corresponding to each receiver coil.

Performing a parallel MRI with the acceleration factor equal to four using the SENSE mechanism is shown in Figure 2.14. The \hat{C} matrix contains the sensitivity information of each receiver coil, whereas the \vec{I} vector contains overlapping pixels that correspond to a certain location in images with a reduced FOV (Blaimer et al., 2004). The overlapped pixels are unfolded using both information to get the final image.

$$\vec{I} = \hat{C} \cdot \vec{p} \quad (2.2)$$

$$\vec{p} = (\hat{C}^H \hat{C})^{-1} \hat{C}^H \cdot \vec{I} \quad (2.3)$$

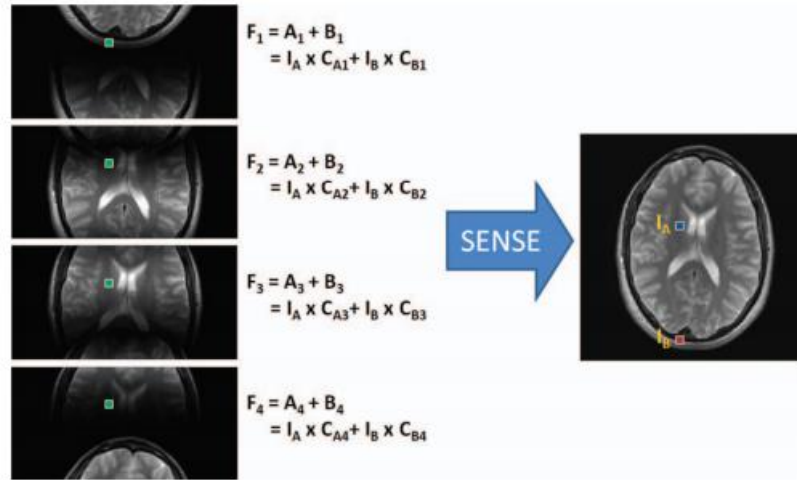


Figure 2.15 The unfolding mechanism of an image with an acceleration factor of two is acquired using a four-channel linear array (Deshmane et al., 2012a)

Acquirement of the unfolded pixels and the composite image with full FOV relies on the matrix inversion shown in Equation 2.3. The notation “H” over matrix \hat{C} denotes the transpose of the complex conjugate matrix, which is named as “Hermitian transpose” or “conjugate transpose” (R. A. Smith, 1968). The inversion matrix is confined by the number of separated pixels and the number of receiver coils. The condition for the SENSE algorithm to work is that the number of superimposed pixels mustn't be greater than the total number of receiver coils (Deshmane et al., 2012). Otherwise the process fails since the matrix operation is not possible to be done. Figure 2.15 shows the unfolding mechanism of an image with an acceleration factor of two for a four coil system.

CHAPTER THREE

MATHEMATICAL MODELS

This section introduces the basic concepts behind each imaging method. The concepts of each imaging system have been clearly outlined. All techniques were executed in an easy-to-understand manner, and each was explained in depth. The working logic of back-projection for CT is described, as well as information regarding the X-ray projection. Additionally, coil configurations for two distinct types of parallel imaging are presented.

3.1 Projection

The theory of X-ray imaging is that radiation is scattered and absorbed when it propagates through an object. Radiation passes in varying levels through an object with differences in thickness or intensity, affecting the image exposure. In X-ray imaging, it is the result of a 2D projection of X-rays due to the attenuating properties of all tissues along their path (Sandborg, 1995). The projection concept example and components of a general radiographic system are shown in Figure 3.1.

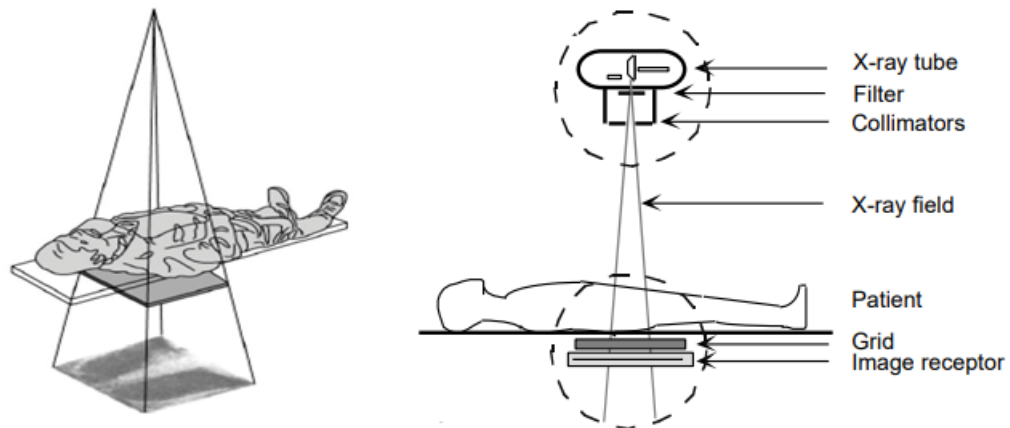


Figure 3.1 Projection sample and imaging device elements (Sandborg, 1995)

The imaging system's components include an X-ray tube, an added filter, a collimator, an anti-scatter grid, and an image receptor. A beam mechanism is used to collimate the photons released by the X-ray tube. The X-ray tube's photons may be scattered, absorbed, or transmitted without causing interference. The image is created of photons that arrive at the receptor (Aichinger et al., 2012).

An electromagnetic radiation type X-ray is capable of passing through the body. When X-rays pass through the body, their energy is absorbed in varying amounts by various areas of the body (Rosendal & Ewertsen, 1952). After the X-rays pass through, a receptor behind the body detects them and transforms them to an image. The white areas in the image represent dense areas such as bone, where X-rays have difficulty passing through. The parts of the body that are most easily penetrated by X-rays, such as the heart and lungs, appear as darker regions as shown Figure 3.2.



Figure 3.2 An example of chest X-ray

3.2 Back-Projection

Tomographic reconstruction is a multidimensional inverse (Kharfi, 2013) problem in which the aim is to estimate a complex structure from limited projections. The back-projection technique has commonly been the most frequently used method for reconstructing images from projections (Suzuki & Yamaguchi, 1988).

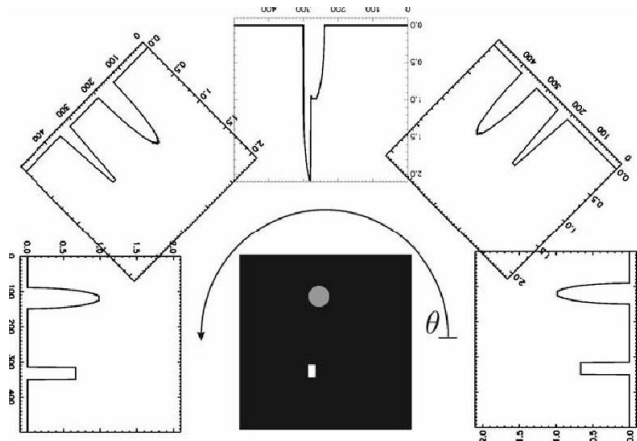


Figure 3.3 The exhibit of projections taken from various angles (Kharfi, 2013)

Projections are obtained with angles between 0 and 180 degrees. Each projection reveals a different feature of the entity, as shown in Figure 3.3. Additionally, the more projections performed, the higher the quality of the final image produced (Kharfi, 2013).

Beginning with a projection value, back-project a ray with equivalent pixel values that sum to that value. The approximate image is then enhanced with the back-projected ray. The procedure is performed for all projections at all angles. The primary issue with back-projection is extreme blurring in the derived images. Thus, there is another reconstruction technique known as filtered back-projection.

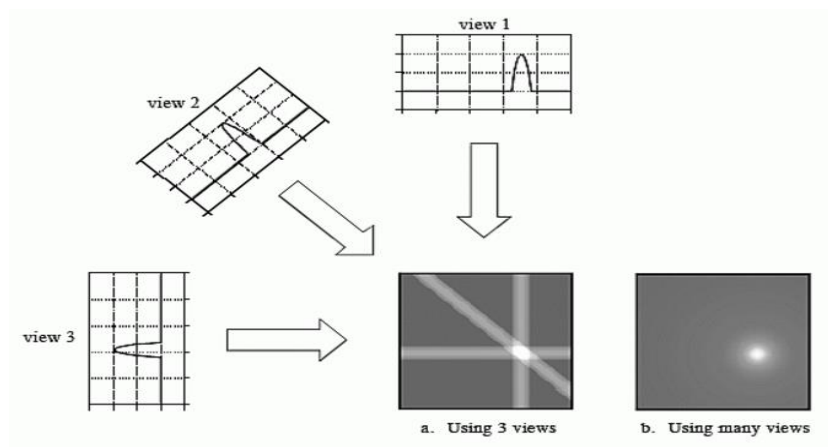


Figure 3.4 Illustration of the back-projection concept (Kharfi, 2013)

Though basic back-projection method is fairly straightforward to grasp, it lacks clarity in terms of images. The main cause of blurring is the overlap of low frequencies, so low frequencies are dominant, as can be seen in Figure 3.4. In filtered-back projection, the clarity of the final image can be increased by suppressing low frequencies by applying a simple ramp filter (Schofield et al., 2020).

3.1 Concept of Parallel Imaging

The gathered MRI information represent in k-space, which includes spatial frequency information, rather than specifically gathering information about the image (Deshmane et al., 2012). Using different magnetic field gradients together with the main magnetic field of the MRI scanner, k-space data is generated. In order to obtain a successful composite image from the data collected in k-space, inverse FT process is applied. Although it is possible to reduce the MRI scan time by collecting less k-space information, it is necessary to solve the spatial overlap problems. To fix this problem, parallel imaging was established.

All parallel imaging techniques have a few features in common. The scan time can be reduced by undersampling the K-space data in the phase coding direction. If the Nyquist condition is not satisfactory, an aliased image is obtained. Data is gathered using differently positioned numerous receiver coils rather than a massive homogenous volume receiver coil. A fully FOV restored image is obtained by using sensitivity maps of the coils together with under-sampled information from each receiver coil for a particular algorithm. (Deshmane et al., 2012).

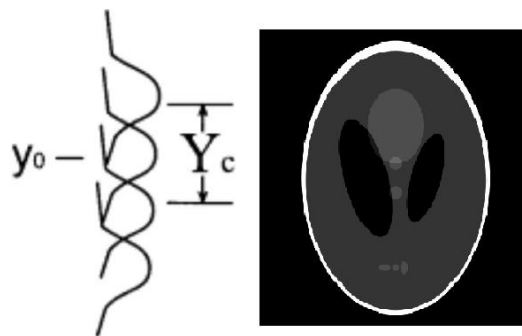


Figure 3.5 Placement of a Coil array placement for PILS (Griswold et al., 2000)

Four receiving coils in the PILS system are placed in the phase coding direction shown in Figure 3.5. The width of each receiver coil's sensitive region is adjusted accordingly same. This variable was denoted by Y_c . The only distinction between receiver coils is the position of the sensitive regions' centers, referred to as y_0 . The distinct location of these receiver coils ensures that each coil encompasses a distinct spatial region in the phase-encoding direction.

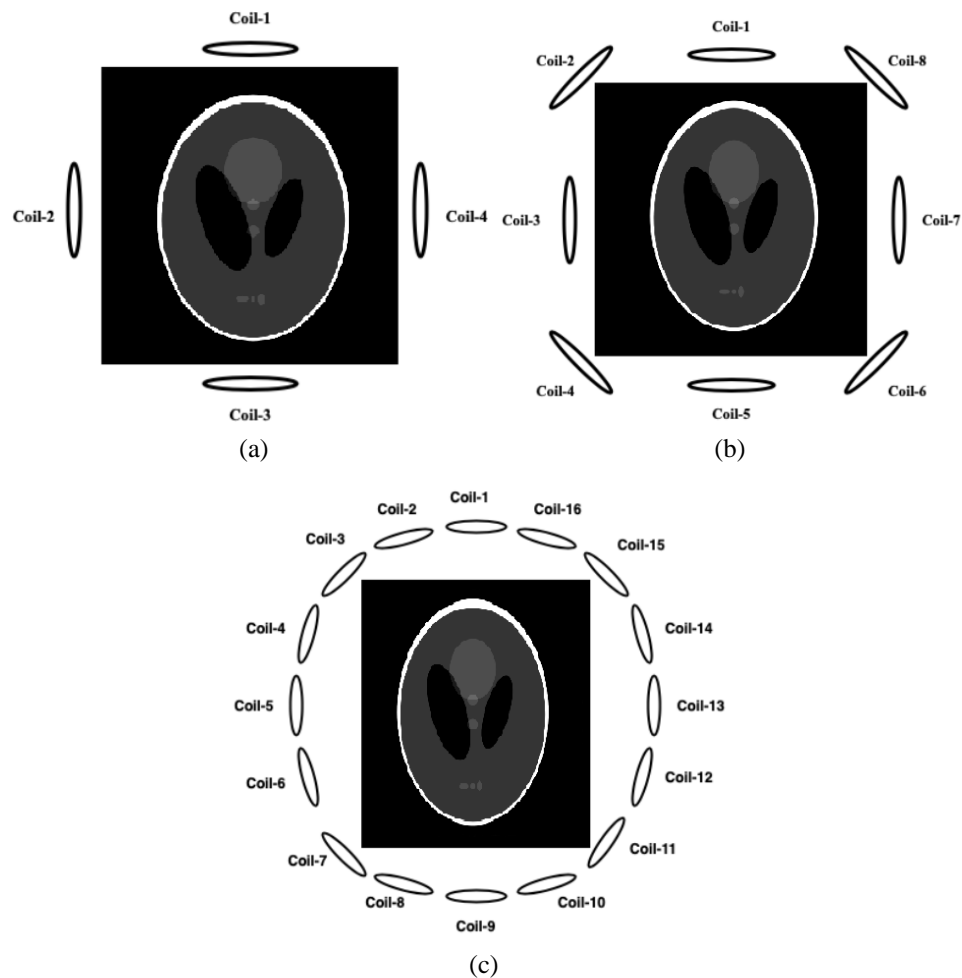


Figure 3.6 Systems of SENSE a) The position of the four receiver coils b) The position of the eight receiver coils c) The position of the sixteen receiver coils

Receiver coils, which are surface coils, were placed in a circular pattern around the imaging object. The enumeration of the receiver coils was implemented in the counter-clockwise direction. For instance, in a set of four-receiver coils positioned around the image, coil 1 is located at clock 12, coil 2 is located at clock 9, coil 3 is located at clock

6, and coil 4 is located at clock 3. This counter-clockwise location configuration, starting from clock 12, was conducted for 4, 8, and 16 receiver coils. Figure 3.6 a shows the coil positions concerning the set of 4 receiver coils, while Figure 3.6 b illustrates the coil positions of the set of 8 receiver coils.

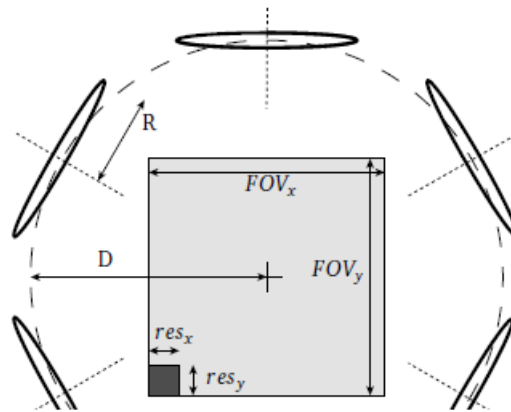


Figure 3.7 Placement of a coil array (Guerquin-Kern, 2012)

One of the MRI simulator (Guerquin-Kern, 2012), the coil array is positioned as shown in Figure 3.7. The adjustable parameters are number of coils, acceleration factor, the radius of coils, and distance from the centers of the coils to the origin. Each parameter affects the quality of reconstructed image. Each coil receives more information from the part of the object closer to it, and this is indicated in each coil's own spatial sensitivity map.

The occupancy of the k-space can be changed with controllable parameters of the simulator. By utilizing an undersampled k-space, the main objective is to produce an unaliased image. Because the occupancy of the k-space is directly proportional to scanning time. On the other hand, if the information in the k-space falls below a certain level, it creates an aliased image. It is to obtain the final image using the sensitivity maps and coil images of each coil.

CHAPTER FOUR

APPLICATIONS AND RESULTS

In this section, the method for X-ray, CT and MRI systems and the results from the same sample will be shown. For each imaging system, all the details are shown step by step and the results are presented.

Since the SL phantom is common to each process, we begin by obtaining the phantom on Matlab. First, 2D SL phantom is created on MATLAB. The size of the 3D phantom is 256x256. Then, 3D SL phantom is created on MATLAB. The size of the 2D phantom is 256x256x256.



Figure 4.1 The 2D SL phantom

The 2D SL phantom is seen in Figure 4.1. The 3D SL phantom is shown in Figure 4.2.

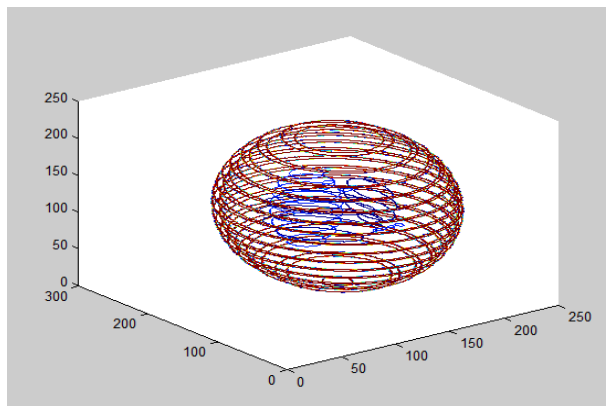


Figure 4.2 The 3D SL phantom on Matlab

4.1 Method and Outcome of X-ray

In the first laboratory application, X-ray application was made for 2D phantom. First, the default phantom was created on matlab. Then, using the attenuation values in Table 2.1, customized phantoms were created. Each selected ellipse at a specific energy level has been tuned to represent a different human tissue such as brain, bone and fat.

In Figure 4.3, the attenuation coefficient map is set so that the different parts are bone, brain, and fat for 60 keV. Required attenuation coefficient values are assigned to the relevant parts.

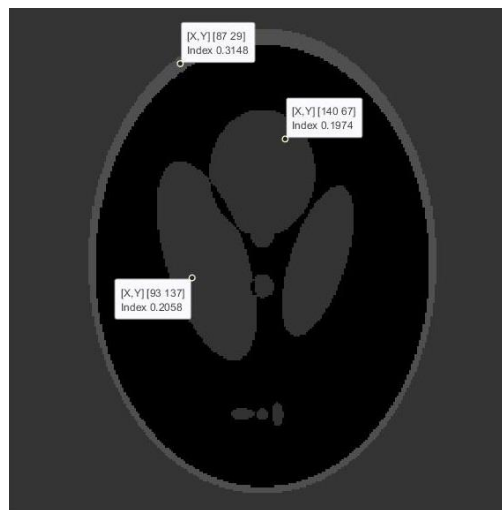


Figure 4.3 The attenuation coefficient maps of 2D phantom

X-ray simply implies a projection; therefore, the projection of a 2D image will be a one-dimensional signal. Using the created attenuation coefficient maps, projection was taken with the help of beer's law. After of all operations, a one-dimensional output was formed as in Figure 4.4.

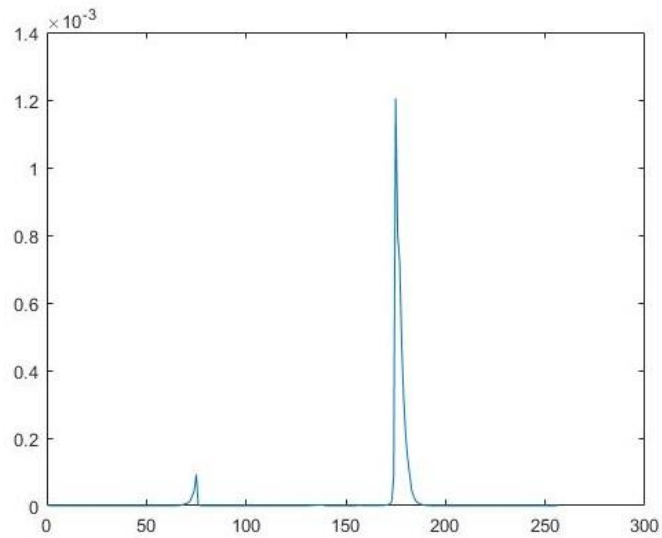


Figure 4.4 Projection of 2D phantom

In the second laboratory study, X-ray application was performed for 3D phantom. After the default phantom was created on matlab, customized phantoms were created using the attenuation values in Table 2.1. For the specific energy level, each selected ellipsoid was adjusted to represent a different human tissue such as brain, bone, muscle and fat. The projection of the 3D phantom was obtained using beer's law from the created attenuation coefficient maps.

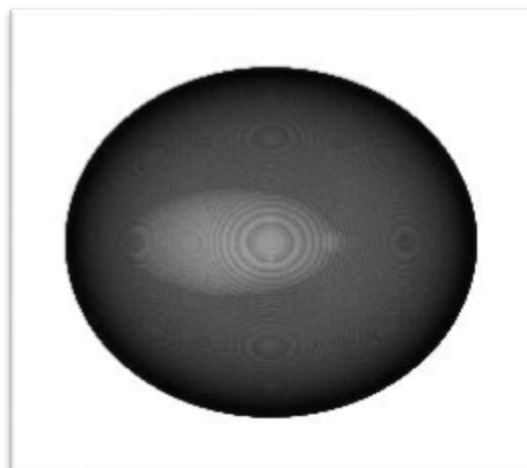


Figure 4.5 Projection of 3D SL phantom

A significant amount of data is lost as a consequence of the projection. Due to the overlapping information, all data in one dimension is merged with data in the other. As a consequence, projecting a 3D sample yields a 2D output as seen in Figure 4.5.

In X-ray imaging, the outcome of a single projection angle is analyzed. By varying the projection angle, different information about the sample may be acquired. This fundamental information serves as the foundation for CT.

4.2 Method and Outcome of CT

A single projection angle offers just restricted information about the object, the total number of projections from various angles should be raised. By increasing the number of projections shot from various angles, more information about the object can be gathered. While raising the number of projections improves the image's quality, an excessive increase might jeopardize people's health. Because an excessive amount of x-ray radiation may be harmful to the human body. Thus, it should be attempted to get the highest quality image feasible with the fewest possible projections, and the optimal projection number should be determined.

Different projections are created for various angles. When performed with one angle range, a total of 180 projections are produced. After all projection procedures are complete, the outputs are compiled into a matrix known as a sinogram. The sinogram in Figure 4.6 is composed of 180 projections made at one-degree gap from a 2D sample.

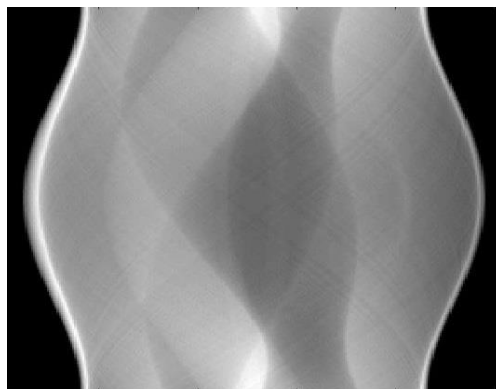


Figure 4.6 Sinogram for 2D SL phantom

While the sinogram may seem meaningless, it contains detailed information about the object. Due to the fact that each projection derived from a different angle, carries specific information about the object. All projections are finished and the sinogram matrix is completed so it can be utilized in the reconstruction process.

Once the sinogram is produced, the reconstruction step can begin, which may be done using a variety of methods. Both the back-projection method and the filtered back-projection techniques have been applied. First, each row of the sinogram representing the projections is extracted independently and put in a distinct matrix, such that each repeats itself. Each matrix is rotated by the projection angle associated with each projection. The sum of the rotated matrices is computed. When all processes have been completed and the final total matrix has been formed, the final image will be constructed.



Figure 4.7 Final image of back-projection method for 2D sample

After all, operations are complete, the acquired final image represent in Figure 4.7. A drawback of the back-projection approach is the increased brightness caused by low-frequency overlap. The filtered back-projection technique was developed to deal with this issue and somehow mitigate the influence of low-frequency components. In contrast to the back-projection approach, an additional filtering step is required. Each projection in the sinogram is filtered separately and processed.

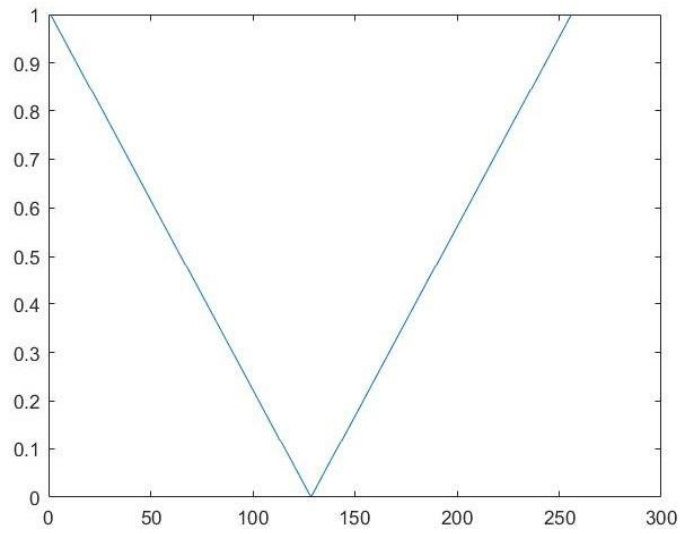


Figure 4.8 Ram-Lak filter

In order to filter the overlapping low-frequency components, the Ramlak filter is used as the high pass filter shown in Figure 4.8. Each sinogram line was filtered with the help of the Ramlak filter. All subsequent steps are the same as the reflection steps. As a consequence, as seen in Figure 4.9, the brightness issue is resolved, and the final image is achieved.

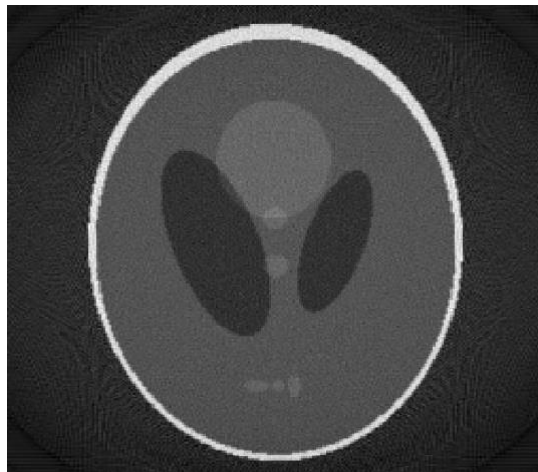


Figure 4.9 Final image of filtered back-projection method for 2D sample

The procedure is identical for the 3D sample, except for the dimensions of the components in the subprocesses. Since the projection output of the 3D phantom is 2D, the sinogram matrix becomes 3D as a result of the combination of these outputs that comprise each sinogram layer. A sinogram composed of 180 projections acquired at a one-degree gap, as seen in Figure 4.10.



Figure 4.10 Sinogram for 3D SL phantom

Each layer of the sinogram is repeated to the size of the object to form a distinct matrix. Each projection's matrix is rotated by the angle of the projection. The final reconstructed image is created by summing all rotated matrices. Since the operation is conducted using 2D matrix projections, the output is 3D, as shown in Figure 4.11.



Figure 4.11 Final output of back-projection method for 3D sample

Figure 4.11 illustrates the final 3D reconstructed image with various operational defects. Nevertheless, it is essential to analyze the subsections in detail to better comprehend everything properly. In Figure 4.12, it is shown that the result of back-projection is represented as a slice plane. It gives the opportunity to examine the final image as axial, sagittal, and coronal slices.

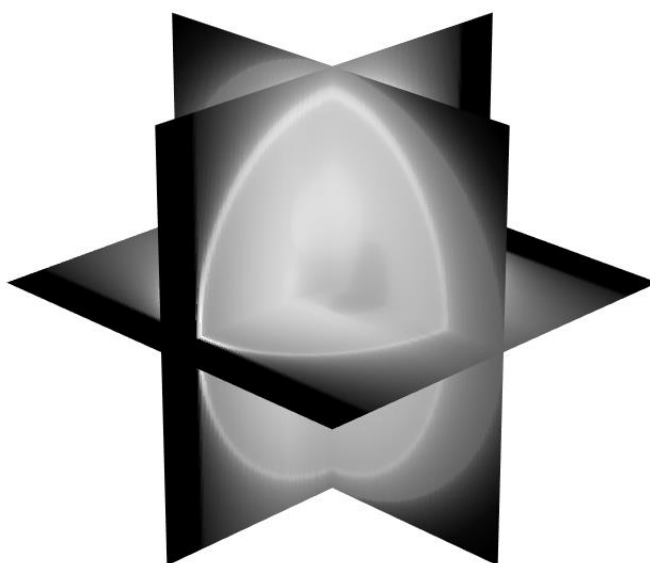


Figure 4.12 The final output of the reconstruction method view as slice plane for the 3D phantom

In Figure 4.13, the axial 120th slice of the back projection result is shown. It is easier to make inferences by examining this intermediate slice. As seen in Figure 4.13, blurring due to the overlapping of low frequencies is seen as a result of back projection. In order to eliminate this resulting turbidity, filtering was performed. Since the projections of the 3D phantom are 2D, each projection was filtered using the high-pass filter seen in Figure 4.14.

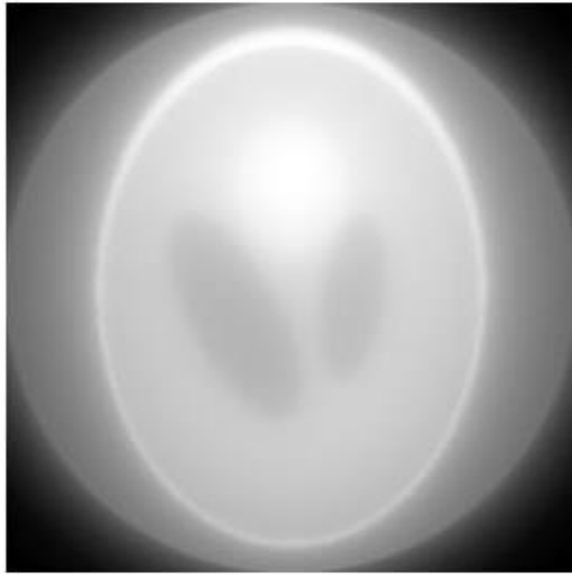


Figure 4.13 120th axial section of back-projection method result

In Figure 4.14, since there is a high-pass filter, the central parts are close to zero, while the outer parts are shown as close to one. From the center to the corners, there is a transition from black to white.

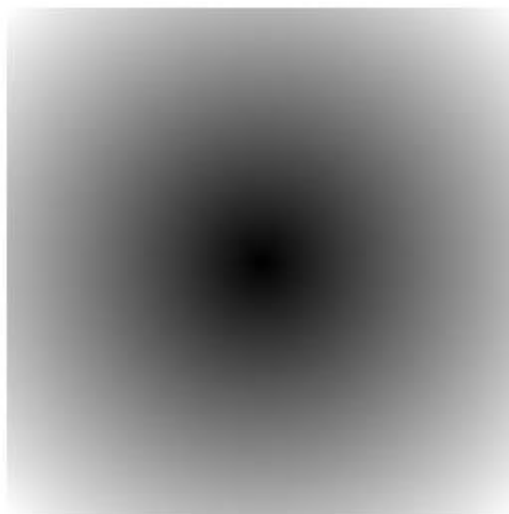


Figure 4.14 The 2D high pass filter

The brightness problem caused by the back projection method is also seen here. When low-frequency components overlap and become dominant, the issue of brightness appears. As in the prior application, this issue can be overcome through filtering.

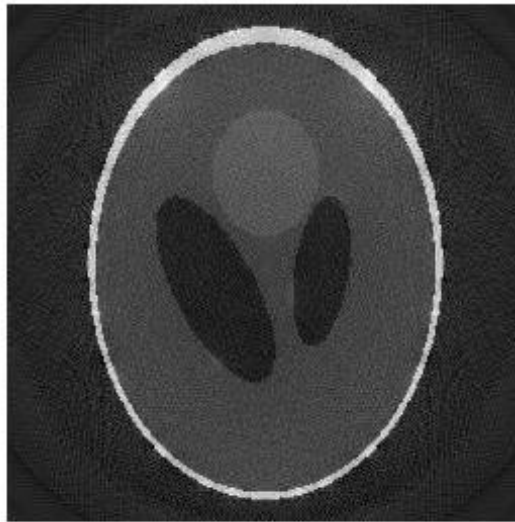


Figure 4.15 120th axial section of back-projection method result

A 2D filter was utilized since each component of the sinogram is 2D. Following the filtering procedure, all operations are identical to those used in the back-projection method. Figure 4.11 seen the 120th axial section of the reconstructed image after the filtered back-projection method procedure is finished. The use of a 2D filter for each projection minimizes the issue of low-frequency component overlapping. Because of the filtering procedure, there seems to be no brightness issue, as seen in Figure 4.11.

4.3 Method and Outcome of PILS

First, for the MRI component, the PILS procedure is performed. The algorithm basically consists of an array of receiver coils, derivation of their sensitivity maps, reduced k-space data for coil images, and a sum-of-squares reconstruction method using these coil images.

The PILS simulation on MATLAB begins by choosing the SL phantom with a matrix size of 256×256 as a reference image. The fundamental coil parameters are artificially produced using MATLAB. Assume that the bandwidth of each receiver coil is equal and that they are positioned in the phase coding orientation as illustrated in Figure 3.6.

Different spatial areas for the receiver coils are created by generating four distinct Gaussian distribution-shaped sensitivity map information. Each Gaussian distribution has the same mean value but a distinct standard deviation, which results in a difference in the sensitive areas covered by each receiver coil. The sensitive areas related to receiver coils with an array set are shown in Figure 4.12. Each color on the graph indicates a different receiver coil; blue is coil 1, purple denotes coil 4.

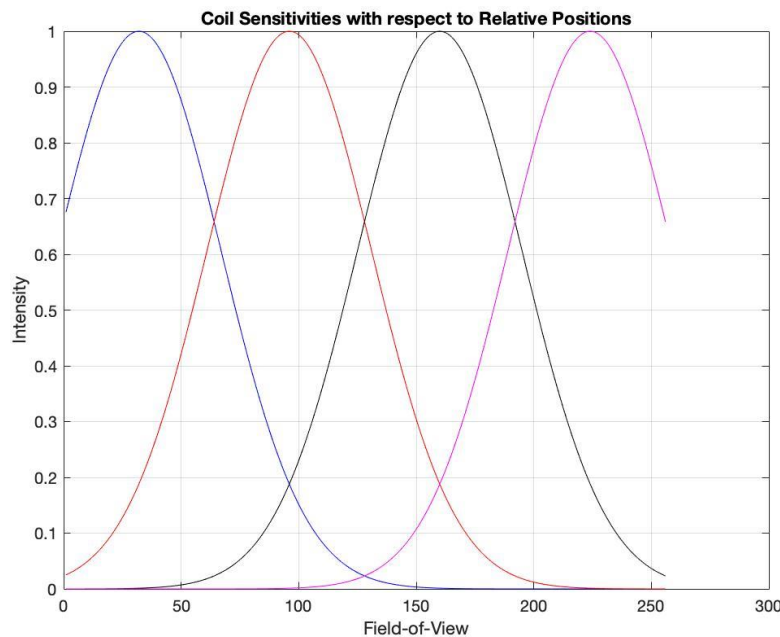


Figure 4.12 Gaussian sensitivity maps corresponding each receiver coil

As seen in Figure 4.13, the sensitivity map of each receiver coil transformed to a matrix format. Each receiving coil is responsible for receiving a signal from a distinct region, and their sensitivity maps are matrixed in accordance with the preceding figure. The white sections indicate the coil's signal reception area.

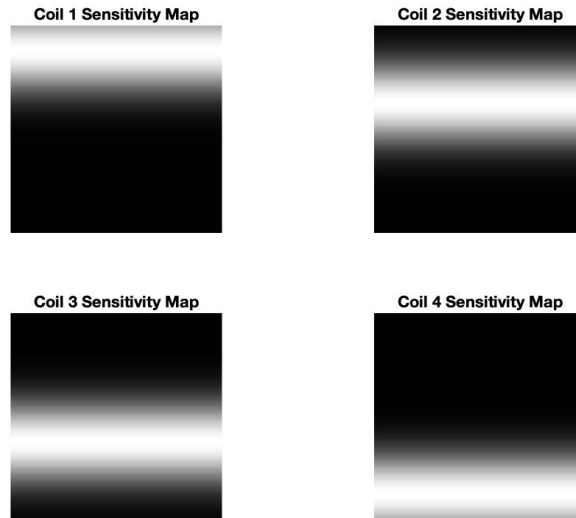


Figure 4.13 Sensitivity map for each receiver coil

A simulation of acquiring MR images with each coil was conducted to see the effect of each receiver coil on the images. Since each receiver coil, in the real-world, is restricted to receive signal in a defined region whose locations are known, same behavior should be obtained on the PILS algorithm simulation on MATLAB. The corresponding coil images for each receiving coil are shown in Figure 4.14.



Figure 4.14 Sensitivity map for each receiver coil

After defining and storing all receiver coil parameters, 2D Fast Fourier Transform (FFT) is used in MATLAB to obtain k-space data. PILS is a parallel MRI method that reconstructs the composite image using undersampled k-space data. Therefore, a process called zero filling was used to perform under-sampling. The rows of the k-space in the form of skipping a row are inserted into the zero vector. Figure 4.15 shows the fully sampled k-space matrices obtained with each receiver coil image, while the Figure 4.16 represents the under-sampled k-space data obtained by zero-filling.

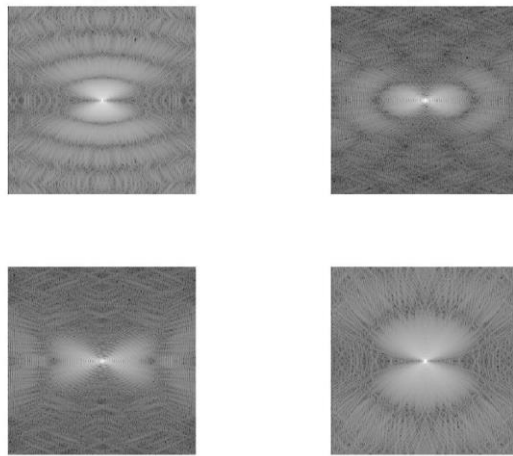


Figure 4.15 Each receiver coil's fully sampled k-space

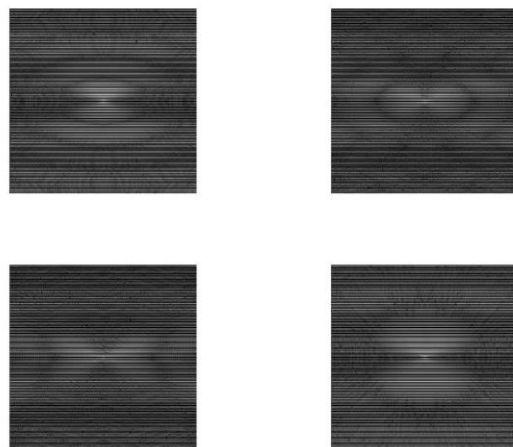


Figure 4.16 Each receiver coil's under-sampled k-space, black lines represent zero-filled lines in the matrix

The transition from undersampled k-space to image space for each coil is accomplished via inverse FFT. As a consequence of the undersampling, the reduced FOV images were seen to be repeated in the image space. A filtering operation was carried out utilizing the sensitivity map of each coil to remove the undesirable periodic recurrence. The images in Figure 4.17 are the consequence of undersampling.

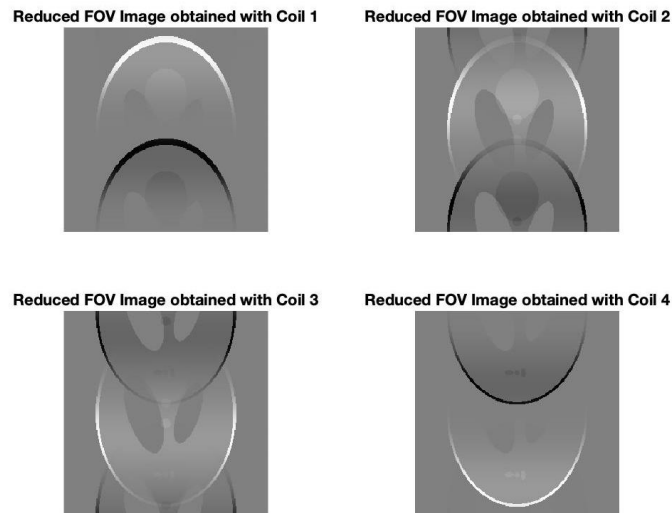


Figure 4.17 Each coil has a reduced FOV image in the form of a periodic repetition.

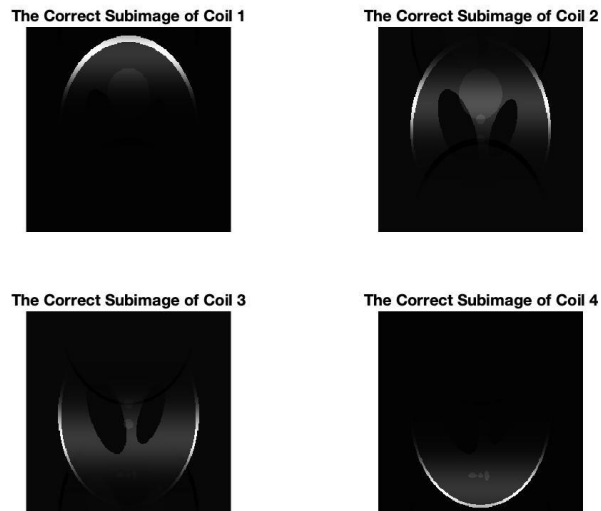


Figure 4.18 The correct subimages that are extracted from periodically repetitive images of each coil.

The correct subimages, shown in Figure 4.18, were extracted by filtering the periodical repetitions with respect to receiver coil locations within the phase-encoding directions. It was guaranteed that utilizable images from each receiver coils were obtained with subsampled k-space data, referring to the acquirement of less k-space information that shortens the duration for data acquisition in MRI.

After extracting the appropriate sub-images, the data set consisted of four distinct images corresponding to each coil. The PILS algorithm's last step is to assemble these images into a single composite image. The composite image is reconstructed by averaging the root mean square of the images acquired with the receiver coils (Unay et al., 2019). This technique computes each pixel value in the composite image by averaging the squares of each pixel extracted from the individual coil images. Figure 4.19 shows the optimal-quality final image that was acquired with the PILS algorithm on MATLAB.



Figure 4.19 The final composite image acquired with PILS algorithm.

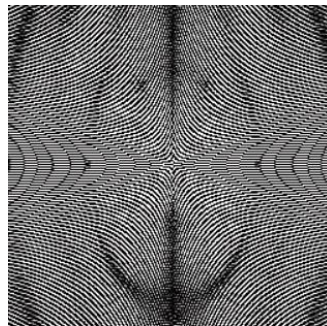
4.3 Method and Outcome of SENSE

During the MRI imaging process, data is gathered in k-space. The occupancy of the k-space is crucial for the reconstructed image quality. The occupancy of the k-space had controlled utilizing a MRI reconstruction simulator's various parameters. The effect of these variables was analyzed also, the SENSE mechanism was implemented using the simulator's undersampled data and variables.

The impacts of coil number, coil radius, distance between coil centers and origin, and reduction factor parameters were all investigated. All other factors in the simulator were kept constant while evaluating the impact of controllable parameters, and the results were seen by altering just the evaluated parameter. The simulator creates the k-space in Figure 4.20 as a result of the default parameter values. The data in the image space can be accessed by using the inverse FFT of the obtained k-space.



(a)



(b)

Figure 4.20 a) Default outcome image for simulator b) k-space of outcome image for simulator

The simulator's coils are all designed to be identical. The error rates of the reconstruction image were investigated by varying the coil radii. While the default coil radius is 0.07 meters, it is initially reduced to 0.01 meters and then increased to 0.13 meters. The results of the error map for each radius value are represented in Figure 4.21. The bar next to each error map indicates the level of the error. Figure 4.21.a shows a minimum level of error at the default coil radius level. In Figure 4.21.b, as the coil radius is decreased, the error rate rises excessively due to the coils receiving limited information. On the other hand, increasing the coil radius in Figure 4.21.c results in a slight increase in error due to mutual inductance.

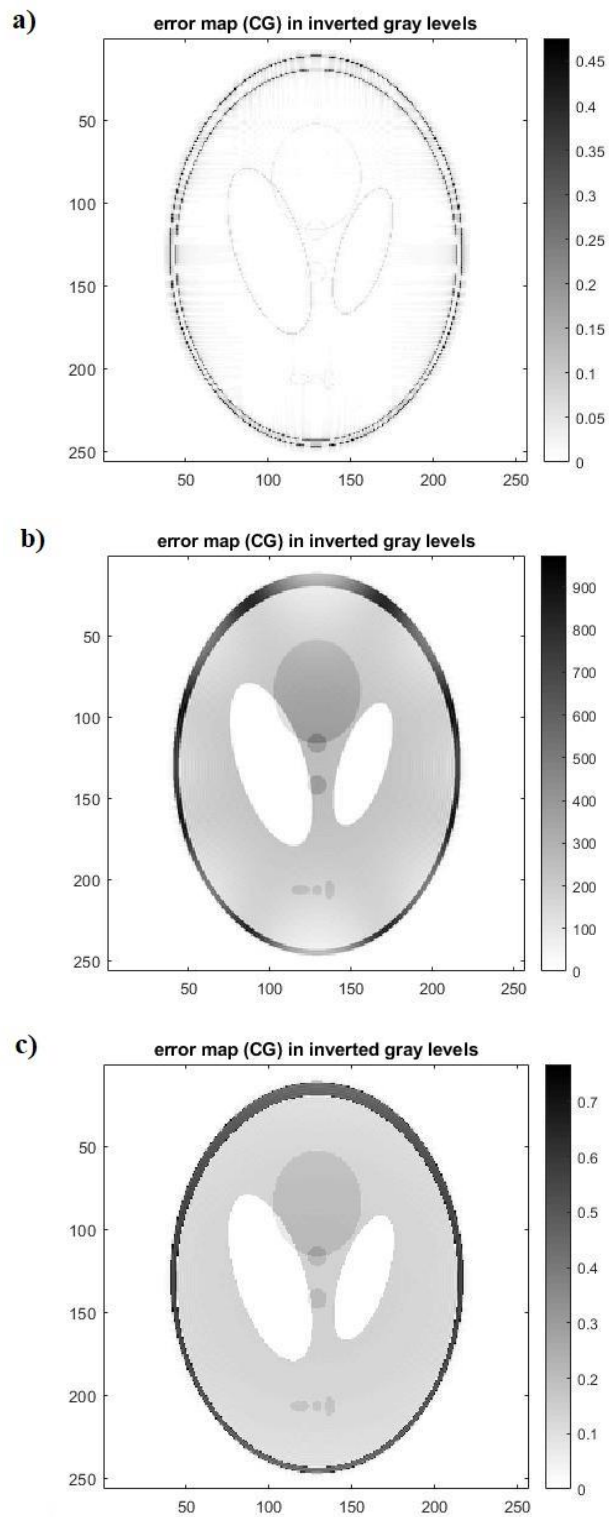


Figure 4.21 a) Error map for default coil radius which is 0.07 m b) Error map for coil radius equal 0.01 m c) Error map for coil radius equal 0.13 m

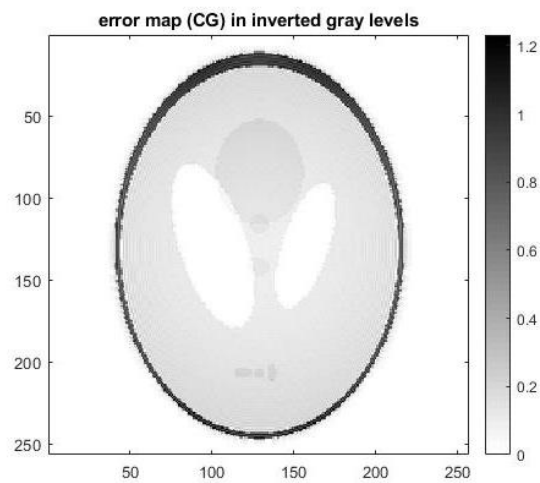
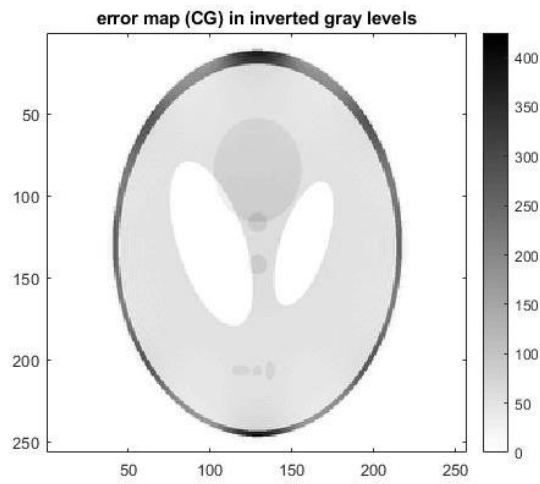
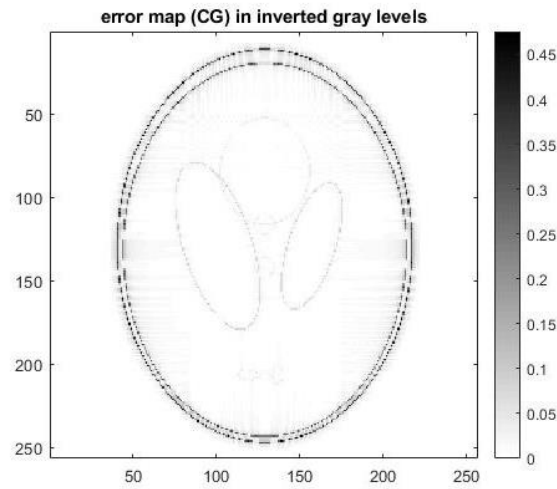


Figure 4.22 a) Error map for default distance from the coils centers to the origin which is 0.17 b) Error map for distance from the coils centers to the origin equal 0.12 c) Error map for distance from the coils centers to the origin 0.22

Each coil is aligned in an equidistant pattern. The distance between the coil centers and the origin was varied to evaluate errors. While the default distance was 0.17 meters, it was first decreased to 0.12 meters before being raised to 0.22 meters. Figure 4.22 illustrates the error maps for all three cases. Figure 4.22 shows the error map obtained by the default distance. As seen in Figure 4.22b, the error climbs dramatically as the distance decreases due to mutual inductance. However, increasing the distance resulted in a slight increase in error in Figure 4.22c. The error was observed due to a decrease in the amount of information received about the object as the coils' distance from the center increased.

The number of coils is another parameter that can be adjusted in the simulator. The number of coils is set to four, eight, and sixteen, respectively. The coil placement in three circumstances is as shown in Figure 3.6, as previously stated. Figure 4.23 illustrates all k-spaces acquired as a consequence of altering coil numbers. The occupancy of the k-space is seen to rise in proportion to the number of coils.

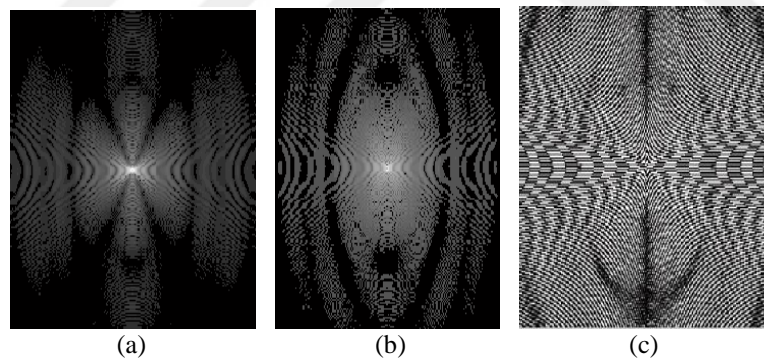


Figure 4.23 a) k-space created by four coils b) k-space created by eight coils c) k-space created by sixteen coils

It has been observed that increasing the number of coils has an impact on the image domain. As seen in Figure 4.24, increasing the number of coils increases the reconstructed image quality considerably. When four coils are used, serious defects occur; however, minor errors occur when eight coils are used. When sixteen coils are used, the sharpest and clearest results are achieved.

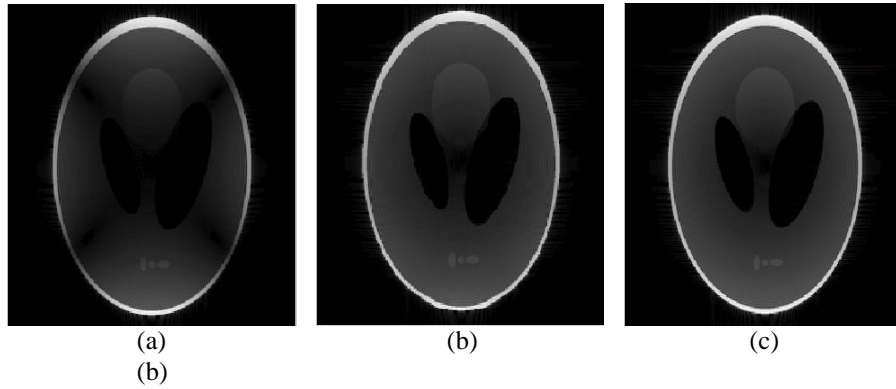


Figure 4.24 a) Image created by four coils b) Image created by eight coils c) Image created by sixteen coils

The last parameter examined is the acceleration factor, also called as the reduction factor. Proportion of the amount of k-space data required for a fully sampled image to the amount received during a faster acquisition known as the acceleration factor. When full sampling is performed, the k-space is completely filled, so the acceleration factor is equal to 1. The occupancy of the k-space reduces with increasing acceleration factor, as seen in Figure 4.25. When the acceleration factor is 2, the k-space occupancy is halved; when the acceleration factor is 4, the k-space occupancy is decreased to one-quarter.

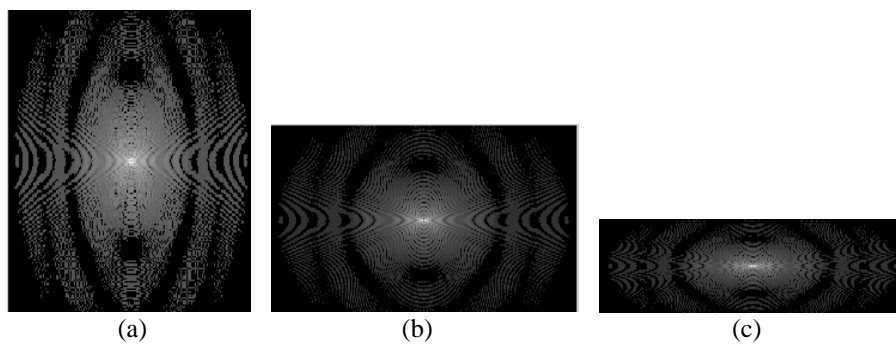


Figure 4.25 a) k-space when the acceleration factor is one b) k-space when the acceleration factor is two c) k-space when the acceleration factor is four

Figure 4.26 illustrates the images produced by varying the acceleration factor. When the acceleration factor is equal to one, no aliasing occurs, as seen in Figure 4.26a. When the acceleration factor is raised, aliasing occurs due to undersampling. As the acceleration factor rises, the amount of aliasing rises as well.

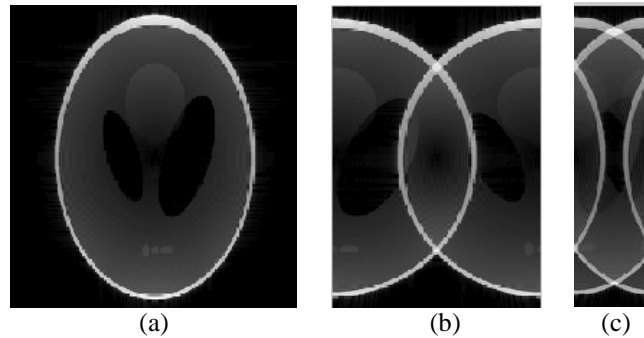


Figure 4.26 a) Image when the acceleration factor is one b) Image when the acceleration factor is two c) Image when the acceleration factor is four

The quantity of information received in k-space reduces as the acceleration factor rises, resulting in a reduction in scanning time. The increase of acceleration factor causes image distortion, however, the acceleration factor should be increased to decrease the scan duration. Different methods have emerged to solve the aliasing problem and reduce the scanning time. A well-known reconstruction approach known as the SENSE approach was carried out.

A four-coil system is demonstrated with all intermediate processes done. The coil placement is as shown in Figure 3.6 a for the system with four receiver coils. The initial step should be to determine the sensitivity map for each receiver coil. As previously stated, each receiver coil can obtain more precise information from the part near it. To exemplify, for a set of four-receiver coils, the first sensitivity map corresponding to the first receiver coil was created in a way that it has proportionally descending values from top to bottom, within the phase-encoding direction. The sensitivity map values increase as going closer to the coil and decrease as getting further away. Sensitivity maps for each coil together are shown in Figure 4.27.

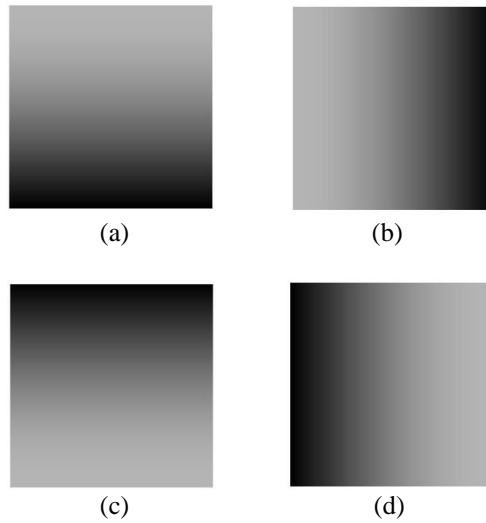


Figure 4.27 Four-receiver coil sensitivity maps (a) represents coil 1, (b) represents coil 2, (c) represents coil 3, and (d) represents coil 4

To show the effect and the sensitive regions of each receiver coil, the reference SL phantom image was multiplied by each sensitivity map as the demonstration which is shown in Figure 4.28. Multiplication of each sensitivity map with the reference SL phantom resulted in weighting the image with the sensitivity map values. It means that each receiver coil image has distinct parts that are brighter or darker, with respect to proximity to the receiver coils.

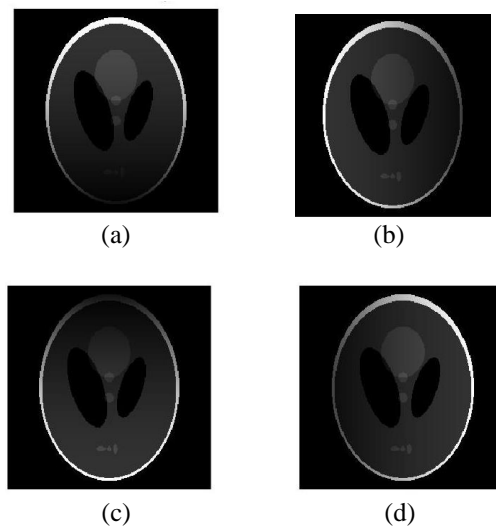


Figure 4.28 Images acquire for each receiver coil with in array; (a) represents coil 1, (b) represents coil 2, (c) represents coil 3, and (d) represents coil 4.

After each receiver coil image is weighted with the corresponding sensitivity map, the next step was to acquire the corresponding k-space data by applying 2D FFT. The 2D FFT provided k-space data that was the same size as the receiver coil images, which were 256×256 in matrix form. In Figure 4.29, the k-spaces of each receiver coil image are shown together.

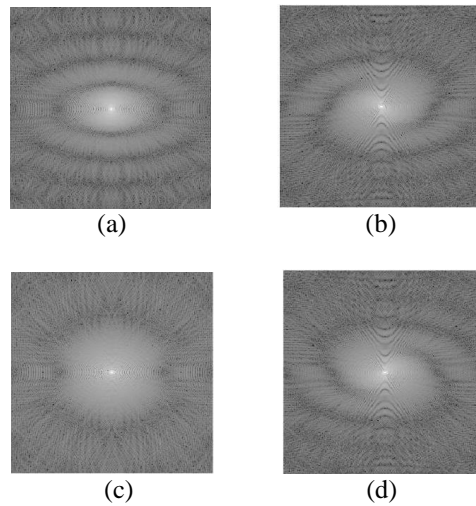


Figure 4.29 Each receiver coil's fully sampled k-space data represented by 256×256 ; (a) represents coil 1, (b) represents coil 2, (c) represents coil 3, and (d) represents coil 4.

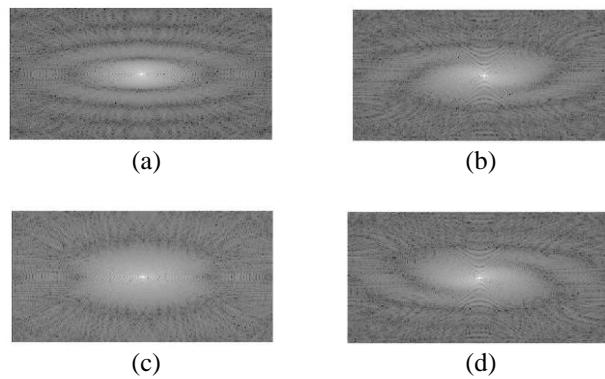


Figure 4.30 Each receiver coil's undersampled k-space data represented by 256×256 ; (a) represents coil 1, (b) represents coil 2, (c) represents coil 3, and (d) represents coil 4.

To simulate undersampling, erase the lines by skipping a line beginning from the top of the k-space, thus increasing the acceleration factor to two. The outcome is a 128x256 matrix with undersampled k-space data as a consequence of this process. In Figure 4.30, the undersampled k-spaces of each receiver coil image are shown together.

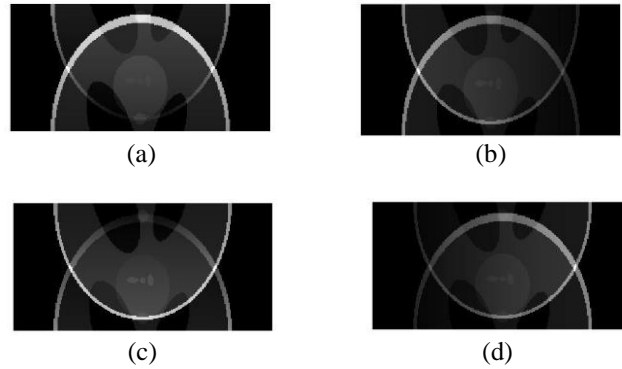


Figure 4.31 Reduced FOV aliased images obtained with acceleration factor equal 2; (a) represents coil 1, (b) represents coil 2, (c) represents coil 3, and (d) represents coil 4.

Each undersampled k-space information is transferred to the image domain using 2D inverse FFT in order to examine the aliasing issue caused by undersampling. The produced undersampled images are 128x256 in size due to the use of 128x256 k-spaces during processing. Coil images of each coil acquired as a consequence of undersampling are presented in Figure 4.31.

Matrix operations are used to unfold each overlapping pixel, as shown in equation 2.3. The defined sensitivity maps and image pixel information are utilized throughout these steps. The final image was obtained after conducting the unfolding operation as shown in Figure 2.16. After the process of aliasing removal via matrix inversion was done, reduced FOV and aliased images turned out to be a composite final image in full FOV. Figure 4.32 shows the final composite image that was reconstructed via the SENSE algorithm with a set of four-receiver coils and an acceleration factor equal to two.



Figure 4.32 Final composite image reconstructed via SENSE with 4 receiver coils and acceleration factor equal 2

The overall SENSE algorithm, whose steps were described above, was repeated for each integer acceleration factor from two to six. Moreover, the sets of 4, 8, and 16 receiver coils were simulated for each acceleration factor. Results of each configuration were stored to compare and evaluate in the next section.

CHAPTER FIVE

COMPARISON

The result of each imaging system will be examined in this section. Each method's pros and cons will be discussed, as well as a comparison. First, an X-ray and CT scan will be compared. Then, after being repeated for various circumstances, PILS and SENSE, which are MRI reconstruction algorithms, will be assessed.

Since the applications of all imaging systems are performed on the same phantom, it is possible to compare each of them. The image formation in each modality can be compared directly. For instance, although the image formation in the x-ray is more practical, the information provided is limited, while CT is based on similar logic, however, is more complex and there is the possibility of creating more detailed images. In MRI, on the other hand, image formation is based on a different principle.

In X-ray and CT, image formation is performed in the image space, while in MRI, raw information is collected in k-space, and then provided information is transformed into the image space. Since X-ray is applied by taking a single projection, it is the imaging method with the shortest scanning time. While the scanning time can be shortened by trying to create an image with the optimum number of projections in order to shorten the length of the scanning process in CT, on the other hand, in the MRI the scanning process is tried to be shortened by reducing the information received in k-space.

It is also possible to compare different dimension results as 2D and 3D applications of each method are performed. In addition to comparing each modality with each other, it has become possible to make comparisons within each modality. For a more detailed comparison, x-ray and CT results were compared with PILS and SENSE for MRI.

5.1 Comparison of X-ray and CT

The x-ray result represented in Figure 5.1 demonstrates that there is a considerable loss of information. Due to the loss of all information in one dimension, all information is overlapped since it is the product of a single projection. Despite the fact that it is just a single projection, it may give useful information about the sample. Although a precise projection angle may be used to distinguish components from one another, determining this particular projection angle is very challenging. Furthermore, acquiring results with a single projection has the advantage of becoming quick and practical. Because the scanning process is so quick, it reduces the amount of radiation exposure as well as the duration gain, making it less damaging to human health than CT.

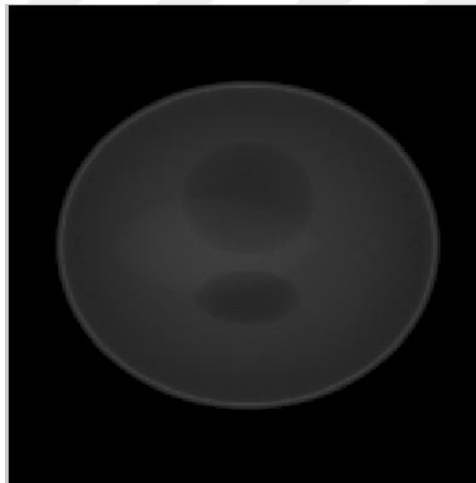


Figure 5.1 X-ray result of 3D SL phantom

In comparison to X-ray, scanning time is quite long due to the many projections obtained at various angles. Due to the high number of projections collected from various angles, information loss is significantly reduced, allowing for the acquisition of more comprehensive 3D information. As seen in Figure 5.2, CT enables the acquisition of more precise and clear images. On the other hand, since the number of projections is many times more than the number of X-rays, the quantity of radiation exposure is much more.

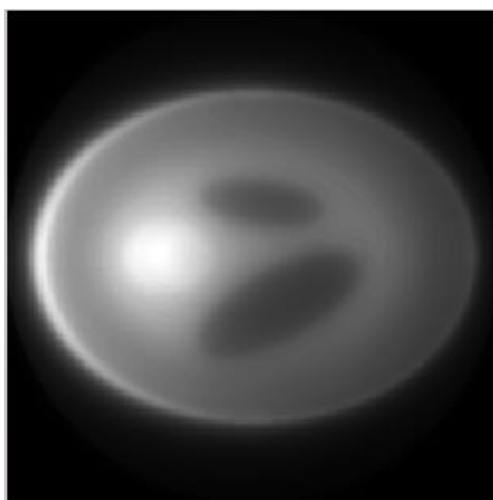


Figure 5.2 Axial section CT result of 3D SL phantom

5.2 Comparison of PILS and SENSE

The results of the two simulations of the PILS and SENSE algorithms were saved in order to compare them. In addition, various coil configurations including distinct sensitive regions and a different number of coil arrangements were derived to interpret the efficacy of the reconstruction algorithm in miscellaneous cases.

Four different composite final images were obtained by using four different receiver coil arrays positioned in the phase coding direction in the PILS algorithm. Gaussian sensitivity maps are created by setting the standard deviation as 30, 35, 40 and 45, respectively. The center of each receiver coil was kept the same for each receiver coil configuration.

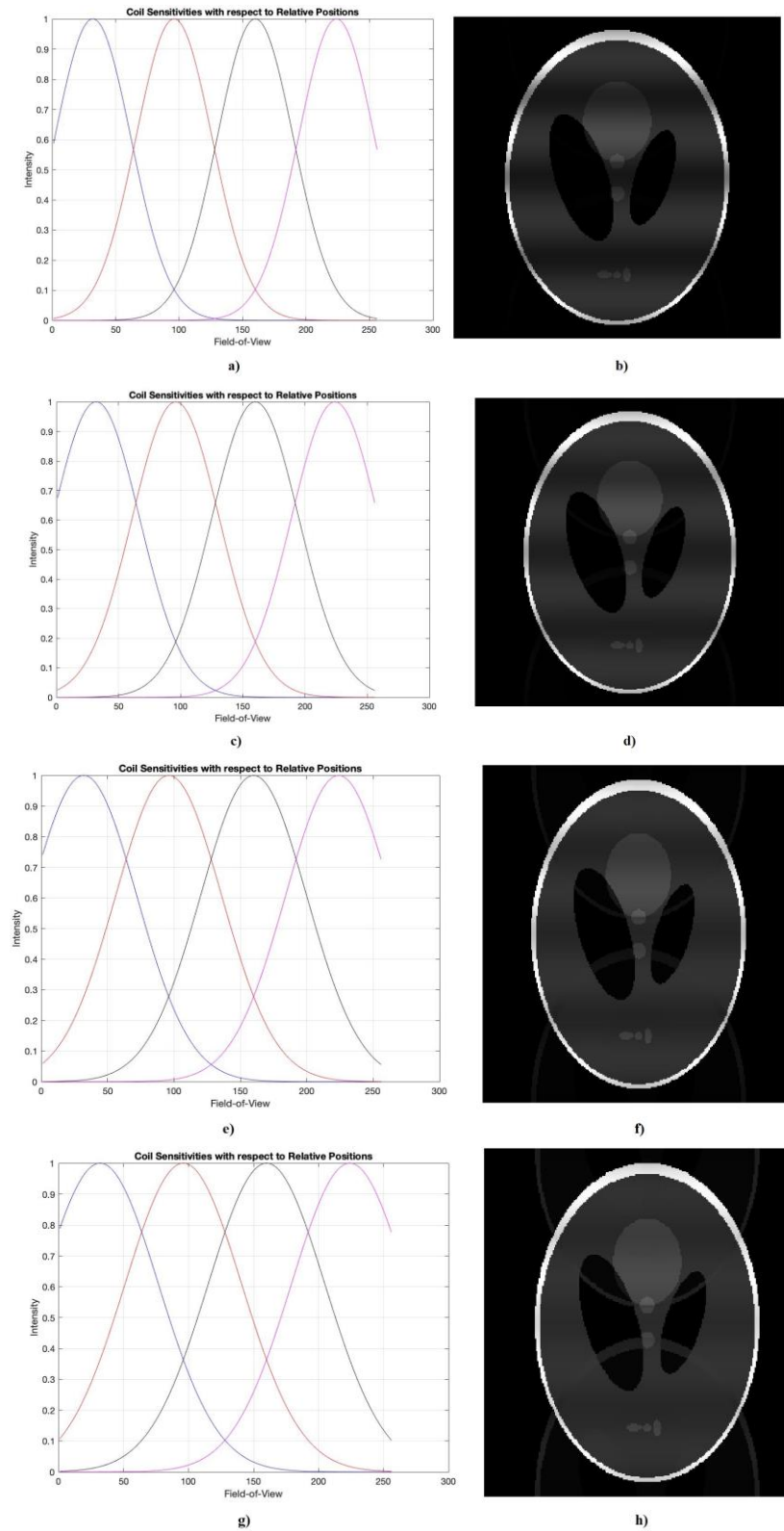


Figure 5.3 Sensitivity maps of each coil acquired with standard deviation equal to a)30 c) 35 e) 40 g)45, The PILS reconstructions for standard deviation equal b)30 d) 35 f) 40 h) 45

Coil sensitivity maps and composite images resulting from reconstruction are shown in Figure 5.3 for each standard deviation value. In each figure showed above, each color in coil sensitivity maps refers to a receiver coil in a way that blue color refers to the coil 1, while the purple color refers to the coil 4. As the standard deviation number rises, the sensitivity bandwidth of the coils expands. On the reconstructed image, this alteration resulted in bands of varied tones.

The PILS reconstruction approach is strongly restricted by coil configurations and placement. Since a receiver coil variables and spatial locations have to be computed and determined before the PILS technique initiate. In real life situations, determining the receive coil variables for PILS can be difficult because the metric variables are the spatial location and center of the receive coils. Any inaccuracy in the variables of the receiver coils can have negative consequences on the reconstructed image acquired by PILS reconstruction in the real world situation.

The total coil numbers are set to four, eight or sixteen respectively and the acceleration value is incrementally increased from two to six for each coil number scenario for the SENSE method. While observing the outcomes of each example, it was noted that some outcomes failed to unfold, some had contrast issues, and some were accurate. Table 5.1 represents the conclusions of each condition.

Table 5.1 The SENSE algorithm's reconstruction outcomes; "A" stands for "accomplished," "CP" stands for "contrast problem ," and "F" stands for "failed in the unfolding process in reconstruction."

Coil number Acceleration factor value	Four Coils	Eight Coils	Sixteen Coils
2	A	A	A
3	CP	CP	CP
4	F	A	A
5	F	CP	CP
6	F	F	CP

The outcomes for each scenario were gathered and included in the table. When the acceleration factor was equal to two, successful results were achieved for each total coil number. In case the acceleration factor is four, the total number of coils should be eight or sixteen to obtain satisfactory results. In all other circumstances, either there is a contrast problem or the SENSE reconstructed images are unsatisfactory for each receive coil configuration. No example with an acceleration factor greater than four produced successful outcomes.

Each of the three different outcomes that emerge from SENSE restructuring is shown below. Figure 5.4 illustrates a failure reconstruction that occurs when the coil number is equal to four and the acceleration factor equal five. When the total coil number is equal eight and the acceleration factor is five, the resulting poor contrast reconstruction is shown in Figure 5.5. Figure 5.6 demonstrates a successful reconstruction with a coil number of sixteen and an acceleration factor of four.

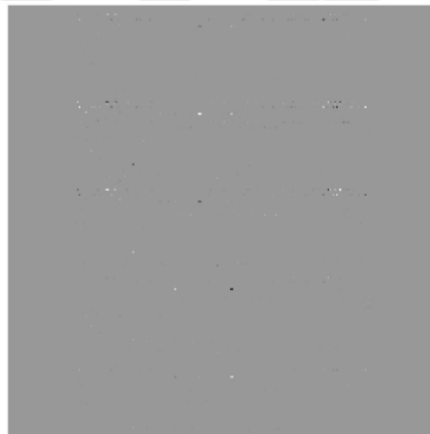


Figure 5.4 The image reconstructed by SENSE had an unfolding problem when the number of coils is four and the acceleration factor is five

The matrix inversion given in Equation 1.4 must be executable for obtaining a successful unfolding mechanism. SENSE reconstruction collapses, resulting in the error as shown in Figure 5.4 for the case where the number of receiver coils is less than the number of overlapping pixels. This is due to the fact that the matrix inversion equation has more unknowns than known variables.



Figure 5.5 The image reconstructed by SENSE had a contrast problem when the number of coils is eight and the acceleration factor is five

The images in several SENSE reconstruction situations were too low in contrast. When the number of receiver coils was insufficient, a high value such as the acceleration factor equal to five could not be tolerated, resulting in this issue. Higher acceleration factors refer to subsampling, which is the process of extracting additional data from the k-space. Because of the overlap problem, as the acceleration factor increases, more pixels begin to fold over one other. To avoid this issue, either raise the acceleration factor or increase the number of receiver coils.



Figure 5.6 The image reconstructed by SENSE had no problem when the number of coils is sixteen and the acceleration factor is four

The receiver coils in the phase coding direction have been seen to restrict the PILS reconstruction method. The final image emerges in a different shape with a small alteration in the receiver coil parameters. On the other hand, the SENSE approach requires only that the coils be positioned counterclockwise around the object. The reliability and flexibility of the SENSE technique at this stage is different from PILS. Thus, the PILS mechanism requires a set of receive coils perfectly positioned in the phase coding direction, which can be difficult to achieve in real world operations. Although the specific parameters of the PILS mechanism prevent its general usage in clinical applications, the SENSE algorithm can operate with an arbitrarily positioned set of receiver coils.

Compared to the PILS reconstruction technique, the SENSE technique gave more accurate results while reconstructing the composite image from undersampled k-space at the same time. The PILS technique is sensitive to slight changes in the sensitivity map and some effects in the form of strip-like forms or aliased regions can be seen on the reconstructed image. The SENSE technique is more commonly used in clinics for the reasons stated.

The speed and duration of the imaging procedure, for both clinics and patient services, are crucial attributes for MRI. Parallel MRI methods such as PILS and SENSE accelerate MR imaging speed by utilizing simultaneous data acquisition with multiple receiver coils. Although there are various variables that determine imaging speed, it is certain the utilization of parallel imaging techniques provides for faster imaging. In the fields of imaging speed and reduction of time to enhance MRI operations, advances are being made every year. The quality and effectiveness of MRI techniques are continually improved.

CHAPTER SIX

IMPLEMENTATION AND EVALUATION

Details about the implementation and evaluation of the designed laboratory will be examined in this section. The objectives for each laboratory will be specified. Pre-laboratory and post-laboratory evaluations will be mentioned. Quantitative results will be evaluated.

The implementation of the designed laboratory was carried out in the Signal and Image Processing Laboratory of Dokuz Eylül University. In total, 9 different experiments were carried out within the scope of the laboratory. Table 6.1 contains all the details of the experiments performed. 13 undergraduate students participated in all experiments.

Table 6.1 Syllabus of designed laboratory

Week	Subject	Experiment
1	Introduction, Basics	Introduction to Laboratory, Matlab and Shepp-Logan Phantom
2	X-ray-1	X-ray Applications of 2D Shepp-Logan Phantom
3	X-ray-2	X-ray Applications of 3D Shepp-Logan Phantom
4	CT-1.1	Translate-Rotate System Pencil Beam X-Ray Projections, Radon Transform, Sinogram
5	CT-1.2	Reconstruction from Projections for Shepp-Logan Phantom: Back-projection and Filtered Back-projection
6	CT-2.1	Three-dimensional Radon Transform
7	CT-2.2	Back-projection and Filtered Back-projection for 3D Shepp-Logan Phantom
8	MRI-1	Imaging in Fourier Space, Limiting Frequency, Nyquist Rate
9	MRI-2	PILS and SENSE mechanisms for the Shepp-Logan phantom

Learning objectives were determined for each designed experiment. The related experiments were designed within the scope of these determined learning objectives. The learning objectives set for each experiment are shown in Table 6.2. A number of learning objectives can vary for each experiment because each experiment focuses on different subjects.

Table 6.2 Objectives of each experiment in designed laboratory

Experiment	Objectives
Introduction, Basics	<ol style="list-style-type: none"> 1. Understanding the laboratory concept and the basics of matlab
X-ray-1	<ol style="list-style-type: none"> 1. Understanding the area of usage for the phantom 2. Understanding why the Shepp-Logan phantom was chosen 3. Understanding concept of X-ray imaging 4. Gaining the ability to take a projection
X-ray-2	<ol style="list-style-type: none"> 1. Understanding the area of usage for the phantom 2. Understanding why the Shepp-Logan phantom was chosen 3. Understanding concept of X-ray imaging 4. Gaining the ability to take a projection of 3D phantom 5. Gain the ability to deal with 3D matrices
CT-1.1	<ol style="list-style-type: none"> 1. Understanding the concept of pencil-beam projections from different angles. 2. Understanding the basics of Radon Transform. 3. Hands on experience on generating a sinogram from projections.
CT-1.2	<ol style="list-style-type: none"> 1. Understanding the concept reconstruction of image slices from projections. 2. Implementing and gaining hands on experience on backprojection. 3. Implementing and gaining hands on experience on filtered backprojection.

Table 6.2 Continues

<p>CT-2.1</p>	<ol style="list-style-type: none"> 1. Understanding radon transform and back projection algorithms in 3D concept 2. Implementing radon transform in volumetric approach
<p>CT-2.1</p>	<ol style="list-style-type: none"> 1. Implementing back projection algorithm to 3D sinogram 2. Implementing filtered back projection algorithm to 3D sinogram
<p>MRI-1</p>	<ol style="list-style-type: none"> 1. To understand the basics and construction of 2-D Fourier space for imaging. 2. Understanding Nyquist rate and limiting frequency (resolution) of an imaging system. 3. Hands-on experience on imaging in (Fourier) K-space. 4. Understanding how noise and other artifacts occur in K-space effects the image space.
<p>MRI-2</p>	<ol style="list-style-type: none"> 1. To understand the basics of reconstruction of parallel imaging. 2. Understanding how the scan time is shortened and the problems that arise in the MRI process. 3. Hands-on experience with PILS algorithm. 4. Hands-on experience with SENSE algorithm.

A total of nine experiments were carried out sequentially. For the evaluation of every experiment except the first experiment, the pre-laboratory and post-laboratory evaluation questions were answered by all students participating in the laboratory. Pre-laboratory and post-laboratory questions are questions that focus on similar points. The pre-laboratory questions, it was aimed to measure the knowledge level of the student before the experiment. The main purpose of answering the post-laboratory questions after each experiment is to measure the students' post-laboratory knowledge level.

Table 6.3 Results of pre-laboratory and post-laboratory evaluation exams (Those marked as '-' in sections represent that students did not take the evaluation exam.)

Lab \ Student	2		3		4		5		6		7		8		9	
	PRE	POST	PRE	POST	PRE	POST	PRE	POST	PRE	POST	PRE	POST	PRE	POST	PRE	POST
1	-	80	35	70	40	15	0	65	0	30	30	60	50	65	0	50
2	35	100	80	80	20	100	30	-	55	60	40	60	-	-	0	90
3	0	90	75	75	30	85	55	-	-	-	40	70	35	70	10	100
4	70	100	80	100	45	100	50	90	-	-	50	90	35	85	30	85
5	0	100	90	100	50	70	55	100	0	100	40	80	100	100	0	90
6	40	100	10	75	60	70	40	90	10	70	40	80	35	70	10	100
7	100	100	100	100	100	100	100	100	100	100	100	100	100	100	20	55
8	65	100	100	100	0	80	30	100	40	50	60	90	70	90	10	20
9	45	95	95	100	60	90	40	90	45	100	30	70	-	-	40	65
10	35	90	50	100	10	70	40	90	75	100	30	60	10	70	30	65
11	100	100	60	90	0	90	40	90	30	70	50	80	100	60	20	35
12	50	90	40	80	60	90	40	65	65	50	50	80	40	70	40	35
13	60	85	95	100	0	55	60	0	55	100	40	70	30	65	-	-
Average	50	95	70	90	36	78	45	88	43	75	46	76	55	77	18	66
Percent Change	%90		%29		%116		%96		%74		%65		%40		%266	

In the first experiment, it was excluded from the evaluation because the concept description of the laboratory was made together with a general introduction. The evaluation results of each student, which were carried out before and after all other experiments, were recorded. All results are shown in Table 6.3. Averages are indicated for each evaluation. For each experiment, the difference between the pre-laboratory exam average and the post-laboratory exam average was calculated.

The most crucial data within the scope of the evaluation is the percentage of change. Because the difference between the students' pre-laboratory evaluation result and post-laboratory evaluation result directly shows how much the student's knowledge level is affected by the laboratory application. After each experiment, the post-evaluation result average was always determined to be greater than the pre-evaluation result average.

The reason for the low percentage of change in the third experiment is that the students in the previous experiment understood the general logic. For this reason, the average of the pre-laboratory evaluation was also high in the third experiment. The difference in later experiments generally decreased because the experiments relatively were more difficult. The fact that the difference ratio was more than fifty percent in all experiments except the third experiment shows that the students benefited from the laboratory practice at a high level. The increase in the accuracy rate of the answers given to the questions created in line with the learning purpose shows that the purpose of the laboratories has been fulfilled.

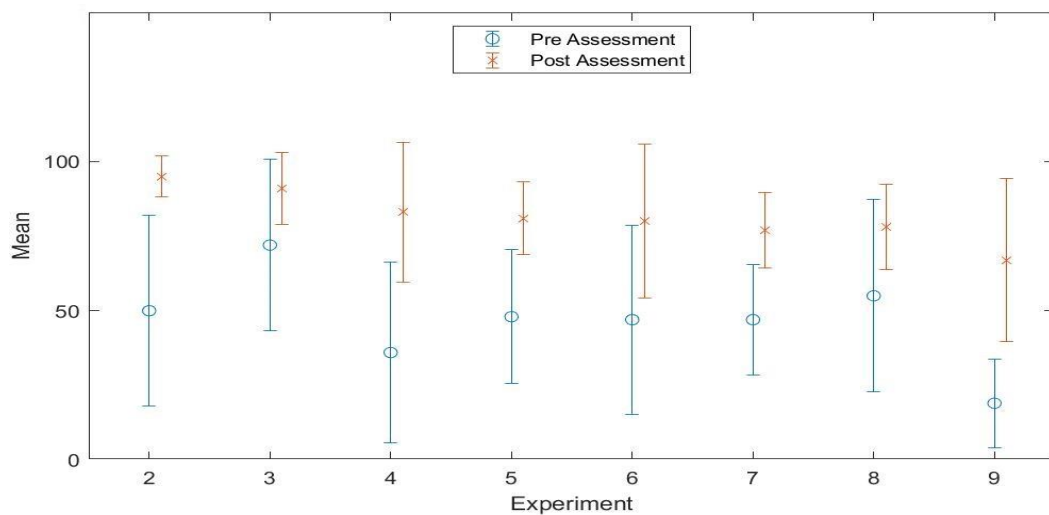


Figure 6.1 The graph of mean and standard deviation for the pre-laboratory assessment and post-laboratory assessment for each experiment. The lines shown represent the standard deviation, the circles represent the pre-laboratory evaluation mean, and the crosses represent the post-laboratory mean for each experiment

As seen in Figure 6.1, the post-laboratory evaluation mean value for each experiment is greater than the pre-laboratory evaluation mean value. Since similar

questions were asked for both evaluations, it was concluded that the students increased their level of knowledge within the scope of laboratory learning objectives after the laboratory. Also, it is often seen that the standard deviation of the pre-laboratory evaluation is greater than the standard deviation of the post-laboratory evaluation. It was observed that the grade distributions of the students were relatively close to each other and their averages were high for post-laboratory evaluation. The reason for the slightly increased standard deviation in the fourth, sixth and ninth experiments is that the related experiments were relatively difficult.

In addition, when the grades of the students are examined, it seems that there is a great difference between the results of the pre-laboratory evaluation and the post-laboratory evaluation of some students. It is observed that the results of the post-laboratory evaluation increase as the lack of knowledge of these students before the laboratory is eliminated during the laboratory. On the other hand, although some students' pre-laboratory evaluation results and post-laboratory evaluation results were also high, it was observed that these students provided more detail in their post-laboratory evaluation answers.

Students can understand the related imaging system application more easily in two-dimensional application within the scope of the laboratory. But since everything is three-dimensional in real life, it has become easier for them to overcome the problems that arise due to the complexity of their three-dimensional applications and to understand the subjects.

After all laboratory applications were completed, the students' feedback was collected. In general, the students stated that they had no difficulty in understanding each imaging system as the experiments progressed gradually in the designed laboratory. They stated that thanks to the pre-evaluation and post-evaluation, they realized their shortcomings and were able to correct their deficiencies in a short time. On the other hand, they complained about the laboratory infrastructure and day planning.

CHAPTER SEVEN

CONCLUSIONS

The main purpose of the thesis is to design a laboratory where students can learn the topics covered in the MIS course practically by using the knowledge they have acquired in the EEE curriculum. In this context, while the projection applications for X-ray are carried out, the back-projection method for CT has been examined. By controlling the occupancy of the k-space for MRI, investigations were made to reduce the scan time as much as possible in order to obtain satisfactory results. Various reconstruction techniques have been performed within the scope of parallel imaging.

Specialized algorithms were created for all modality applications using the 2D SL phantom as an example. In addition, special algorithms have been created to perform X-ray and CT applications in 3D, which is not frequently applied. Since the SL phantom is used for all applications, the details can be observed by comparing all the results obtained. By performing processes for all possible situations, the effect of each can be observed. In this way, it has become easier for students to compare and understand all imaging techniques, as well as to obtain detailed information about the specific imaging system.

In this study, three different imaging systems, namely X-ray, CT, and MRI, were probed, and simulations of each were examined on the same sample. Thanks to the flexibility of the designed laboratory, it can be expanded the scope by making various additions. New imaging modalities can be added for further studies without changing the laboratory concept. It can also be incorporated into laboratory work to examine different reconstruction methods. Future laboratory work may include the iterative reconstruction method for CT, the simultaneous acquisition of spatial harmonics (SMASH), and the generalized autocalibrating partially parallel acquisitions (GRAPPA) methods for MRI.

REFERENCES

- Ahmad, M., Pratz, G., Bazalova, M., & Xing, L. (2014). X-ray luminescence and X-ray fluorescence computed tomography: New molecular imaging modalities. *IEEE Access*, 2, 1051–1061.
- Aichinger, H., Joite-Barfuß, S., Dierker, J., & Sabel, M. (2012). *Radiation exposure and image quality in X-Ray diagnostic radiology: Physical principles and clinical applications*, (2nd ed.), 1–307, Berlin: Springer.
- Alexiadis, D. S., & Mitianoudis, N. (2013). MASTERS: A virtual lab on multimedia systems for telecommunications, medical, and remote sensing applications. *IEEE Transactions on Education*, 56(2), 227–234.
- Alg, O., & Atalar, E. (2015). Manyetik rezonans görüntüleme fiziği. *Temel Radyoloji*, 21, 1–28.
- Assumus, A. (1995). Early history of X-Rays. *Beam Line*, 10–24.
- Beckmann, E. C. (2006). CT scanning the early days. *British journal of radiology*, 79(937), 5–8.
- Berger, A. (2002). How does it work?: Magnetic resonance imaging. *BMJ*, 324(7328), 35–35.
- Blaimer, M., Breuer, F., Mueller, M., Heidemann, R. M., Griswold, M. A., & Jakob, P. M. (2004). SMASH, SENSE, PILS, GRAPPA. How to choose the optimal method. *Topics in Magnetic Resonance Imaging*, 15(4), 223–236.
- Boesch, C. (2004). Nobel prizes for nuclear magnetic resonance: 2003 and historical perspectives. *Journal of Magnetic Resonance Imaging*, 20(2), 177–179.
- Bottomley, P. A., Foster, T. H., Argersinger, R. E., & Pfeifer, L. M. (1984). A review of normal tissue hydrogen NMR relaxation times and relaxation mechanisms from 1-100 MHz: Dependence on tissue type, NMR frequency, temperature, species, excision, and age. *Medical Physics*, 11(4), 425–448.
- Chan, R. W., Lau, J. Y. C., Lam, W. W., & Lau, A. (2018). Magnetic resonance

- imaging. In R. Narayan, (Ed.). *Encyclopedia of biomedical engineering* (3rd ed.) (574-588). North Carolina: Elsevier.
- Cheng, G. K., Sarlls, J. E., & Özarlan, E. (2007). Three-dimensional analytical magnetic resonance imaging phantom in the fourier domain. *Magnetic Resonance in Medicine*, 58(2), 430–436.
- Cooper, G. M. (2000). *The Cell: A molecular approach* (2nd ed). Sunderland (MA): Sinauer associates.
- Cormack, A. M. (1964). Representation of a function by its line integrals, with some radiological applications. II. *Journal of Applied Physics*, 35(10), 2908–2913.
- Deshmane, A., Gulani, V., Griswold, M. A., & Seiberlich, N. (2012). Parallel MR imaging. *Journal of Magnetic Resonance Imaging*, 36(1), 55–72.
- Dikshit, A., Wu, D., Wu, C., & Zhao, W. (2005). An online interactive simulation system for medical imaging education. *Computerized Medical Imaging and Graphics*, 29(6), 395–404.
- Gach, H. M., Tanase, C., & Boada, F. (2008). 2D and 3D Shepp-logan phantom standards for MRI. *Proceedings of 19th international conference on systems engineering, ICSEng 2008*, 521–526.
- Glatard, T., Lartizien, C., Gibaud, B., Da Silva, R. F., Forestier, G., Cervenansky, F., Alessandrini, M., Benoit-Cattin, H., Bernard, O., Camarasu-Pop, S., Cerezo, N., Clarysse, P., Gaignard, A., Hugonnard, P., Liebgott, H., Marache, S., Marion, A., Montagnat, J., Tabary, J., & Friboulet, D. (2013). A virtual imaging platform for multi-modality medical image simulation. *IEEE Transactions on Medical Imaging*, 32(1), 110–118.
- Griswold, M. A., Jakob, P. M., Nittka, M., Goldfarb, J. W., & Haase, A. (2000). Partially parallel imaging with localized sensitivities (PILS). *Magnetic Resonance in Medicine*, 44(4), 602–609.
- Guerquin-Kern, M. (2012). *Matlab code for MRI simulation and reconstruction*. Retrieved June 26, 2021, from <http://bigwww.epfl.ch/algorithms/mri-reconstruction>.

- Guerquin-Kern, M., Karahanoğlu, F. I., Van De Ville, D., Pruessmann, K. P., & Unser, M. (2010). Analytical form of Shepp-Logan phantom for parallel MRI. *2010 7th IEEE International symposium on biomedical imaging: from nano to macro, ISBI 2010 - proceedings*, 4, 261–264.
- Guerquin-Kern, M., Lejeune, L., Pruessmann, K. P., & Unser, M. (2012). Realistic analytical phantoms for parallel magnetic resonance imaging. *IEEE Transactions on Medical Imaging*, 31(3), 626–636.
- Haidekker, M. A. (2013). *Medical imaging technology*. New York: Springer.
- Hounsfield, G. N. (1973). Computerized transverse axial scanning (tomography): Part I. description of system. *British Journal of Radiology*, 46(552), 1016–1022.
- Hounsfield, G. N. (1980). Computed medical imaging. *Medical Physics*, 7(4), 283–290.
- Kaçar, S., & Bayilmis, C. (2013). A web-based educational interface for an analog communication course based on MATLAB builder NE with webfigures. *IEEE Transactions on Education*, 56(3), 346–354.
- Kalender, W. A. (2006). X-ray computed tomography. *Physics in Medicine and Biology*, 51(13), 29–43.
- Kharfi, F. (2013). Mathematics and physics of computed tomography (CT): demonstrations and practical examples. In *Imaging and radioanalytical techniques in interdisciplinary research* (81-107). Croatia: InTech.
- Kharzeev, D. E., Landsteiner, K., Schmitt, A., & Yee, H.-U. (2012). “Strongly Interacting Matter in Magnetic Fields”: An Overview, 871, 1–11.
- Konez, O. (1995). Atomik partiküller ve manyetizma. Manyetik rezonans görüntüleme Retrieved June 26, 2021, from http://www.konez.com/atomic_particles.htm.
- Kumar, A. (2014). History of MRI. *Journal of the Indian Institute of Science*, 94(4), 363–370.
- Lauterbur, P. C. (1973). Image formation by induced local interactions: examples employing nuclear magnetic resonance. *Nature*, 242, 190–191.

- Ledoux, P., Kind, M., Le Loarer, F., Stoeckle, E., Italiano, A., Tirode, F., Buy, X., & Crombé, A. (2019). Abnormal vascularization of soft-tissue sarcomas on conventional MRI: Diagnostic and prognostic values. *European Journal of Radiology*, *117*, 112–119.
- Mikla, V. I., Rusin, V. I., & Boldizhar, P. A. (2012). Advances in imaging from the first X-Ray images. *Journal of Optoelectronics and Advanced Materials*, *14*(7–8), 559–570.
- Mohan, K. A., Panas, R. M., & Cuadra, J. A. (2020). SABER: A systems approach to blur estimation and reduction in X-Ray imaging. *IEEE Transactions on Image Processing*, *29*, 7751–7764.
- Paschal, C. B. (2003). The need for effective biomedical imaging education. In *IEEE Engineering in Medicine and Biology Magazine*, *22*(4), 88-91.
- Paschal, C. B., & Morris, H. D. (2004). K-Space in the Clinic. *Journal of Magnetic Resonance Imaging*, *19*(2), 145–159.
- Paschal, C. B., Nightingale, K. R., & Ropella, K. M. (2006). Undergraduate biomedical imaging education. *Annals of Biomedical Engineering*, *34*(2), 232–238.
- Prince, J., & Links, J. (2006). *Medical imaging signals and systems*. Upper Saddle River: Pearson Prentice Hall.
- Roemer, P. B., Edelstein, W. A., Hayes, C. E., Souza, S. P., & Mueller, O. M. (1990). The NMR phased array. *Magnetic Resonance in Medicine*, *16*(2), 192–225.
- Rosendal, T., & Ewertsen, H. (1952). Roentgen examination of the temporal bone for cholesteatoma. *Acta Radiologica*, *37*(5), 431–444.
- Sandborg, M. (1995). *Radiography and fluoroscopy: Physical principles and biohazards*. Retrieved July 29, 2021, from Linköping University Electronic Press website: <http://urn.kb.se/resolve?urn=urn:nbn:se:liu:diva-57762>
- Schofield, R., King, L., Tayal, U., Castellano, I., Stirrup, J., Pontana, F., Earls, J., & Nicol, E. (2020). Image reconstruction: Part 1 – understanding filtered back

- projection, noise and image acquisition. *Journal of Cardiovascular Computed Tomography*, 14(3), 219–225.
- Selver, M.A. (2015), Design and Configuration of a Medical Imaging Systems Computer Laboratory Syllabus. *IEEE Transactions on Education*, 59.2 (2015): 129-136.
- Seyyedi, S. (2018). *Advanced reconstruction and noise reduction techniques in four- and six-dimensional X-ray imaging modalities*, Phd Thesis, Technical University of Munich, Munich.
- Shepp, L. A., & Kruskal, J. B. (1978). Computerized tomography: the new medical X-Ray technology. *The American mathematical monthly*, 85(6), 420–439.
- Shepp, L. A., Logan, B. F., & Hill, M. (1974). The fourier reconstruction of a head section. *IEEE Transactions on Nuclear Science*, 21–43.
- Smith, M. R., Chen, L., Hui, Y., Mathews, T., Yang, J., & Zeng, X. (1997). Alternatives to the use of the DFT in MRI and spectroscopic reconstructions. *International Journal of Imaging Systems and Technology*, 8(6), 558–564.
- Smith, R. A. (1968). Matrix Equation $XA + BX = C$. *SIAM J. Appl. Math.*, 16(1), 198–201.
- Sonka, M., Dove, E. L., & Collins, S. M. (1998). Image systems engineering education in an electronic classroom. *IEEE Transactions on Education*, 41(4), 263–272.
- Stanisz, G. J., Odobina, E. E., Pun, J., Escaravage, M., Graham, S. J., Bronskill, M. J., & Henkelman, R. M. (2005). T1, T2 relaxation and magnetization transfer in tissue at 3T. *Magnetic Resonance in Medicine*, 54(3), 507–512.
- Stanley, R. J., Watkins, S. E., Gopal, A., & Moss, R. H. (2004). A web-shareable real-world imaging problem for enhancing an image-processing curriculum. *IEEE Transactions on Education*, 47(2), 211–219.
- Suzuki, S., & Yamaguchi, S. (1988). Comparison between an image reconstruction method of filtering backprojection and the filtered backprojection method. *Applied Optics*, 27(14), 2867.

- Tekin, H. O., Singh, V. P., Altunsoy, E. E., Manici, T., & Sayyed, M. I. (2017). Mass attenuation coefficients of human body Organs using MCNPX Monte Carlo Code. *Iranian Journal of Medical Physics*, 14(4), 229–240.
- Unay, M., Kavur, A. E., Agir, B. K., Zoral, E. Y., & Selver, M. A. (2019). *Design of a computer experiment for analyzing the effects of gradient and RF coils during K - space acquisition*. 4–5, Paris, France.
- Veena. T, D. V. Chidanand, K. A. & K. (2015). Quality analysis of mango fruit with fruit fly insect by non-destructive soft X-Ray method. *International Journal of Agricultural Science and Research (IJASR)*, 5(3), 37–46.
- Villarraga-Gómez, H., Herazo, E. L., & Smith, S. T. (2019). X-ray computed tomography: from medical imaging to dimensional metrology. *Precision Engineering*, 60, 544–569.
- Walle, R. Van De, Barrett, H. H., Cornelis, J., Altbach, M. I., Desplanques, B., Gmitro, A. F., & Lemahieu, I. (2000). Reconstruction of MR images from data acquired on a general nonregular grid by pseudoinverse calculation. *IEEE Transactions on Medical Imaging*, 19(12), 1160–1167.
- Wang, L. (2017). *Fast and Accurate 3D X-ray image reconstruction for non destructive test industrial applications*. Phd Thesis, Paris-Saclay University, Paris.
- Wilhjelm, J. E., Pihl, M. J., Lonsdale, M. N., & Jensen, M. (2008). An active learning approach to the physics of medical imaging. *Medical Engineering and Physics*, 30(5), 607–614.
- Zho, Z. H., Jones, J., & Singh, M. (1993). *Foundations of medical imaging*. New York: Wiley.